Inorganic Chemistry
Cite This: Inorg. Chem. 2018, 57, 15079−15092
Article
pubs.acs.org/IC

Synergistic Effect between Different Coordination Geometries of Lanthanides and Various Coordination Modes of 2-Picolinic Acid Ligands Tuning Three Types of Rare 3d−4f Heterometallic Tungstoantimonates

Yanhong Chen, Longhui Sun, Shenzhen Chang, Lijuan Chen,* and Junwei Zhao*

Henan Key Laboratory of Polyoxometalate Chemistry, College of Chemistry and Chemical Engineering, Henan University, Kaifeng, Henan 475004, People's Republic of China

Supporting Information

ABSTRACT: Three types of N-heterocyclic aromatic acid decorated 3d−4f heterometallic Keggin-type tungstoantimonates: $Na_4[Ln(H_2O)_5]_2[Fe_4(H_2O)_2(pic)_4(B\text{-}\beta\text{-}SbW_9O_{33})_2]\cdot 26H_2O$ [Ln^{3+} = La^{3+} (**1**), Pr^{3+} (**2**), Nd^{3+} (**3**), Sm^{3+} (**4**), Eu^{3+} (**5**)], $Na_6H_4[Fe_2W_4O_9(H_2O)_2(Hpic)_4(B\text{-}\beta\text{-}SbW_9O_{33})_2][Ln(H_2O)_8]_2[Fe_4W_2O_7(H_2O)_4(pic)_2(Hpic)_2(B\text{-}\beta\text{-}SbW_9O_{33})_2]\cdot 38H_2O$ [Ln^{3+} = Gd^{3+} (**6**), Dy^{3+} (**7**)], and $Na_2H_2\{[Ln(H_2O)_6]_2[Fe_4(H_2O)_2(Hpic)_2(pic)_2(B\text{-}\beta\text{-}SbW_9O_{33})_2]\}_2\cdot 44H_2O$ [Ln^{3+} = Ho^{3+} (**8**), Er^{3+} (**9**), Hpic = 2-picolinic acid] have been prepared. **1**−**5** comprise a quadripic-inserted Krebs-type $[Fe_4(H_2O)_2(pic)_4(B\text{-}\beta\text{-}SbW_9O_{33})_2]^{10-}$ moiety supported by two $[Ln(H_2O)_5]^{3+}$ groups on both sides where it can be considered that four pic ligands replace eight aqua ligands located on the original Krebs-type $[Fe_4(H_2O)_{10}(B\text{-}\beta\text{-}SbW_9O_{33})_2]^{10-}$ fragment to form the $[Fe_4(H_2O)_2(pic)_4(B\text{-}\beta\text{-}SbW_9O_{33})_2]^{10-}$ moiety. Remarkably, the quadripic-inserted subunits are further concatenated through the coordination role of the pic ligands to create a 3-D heterometallic framework. In contrast, the molecular units of **6**−**7** contain two kinds of non-Krebs-type quadripic-inserted $[Fe_2W_4O_9(H_2O)_2(Hpic)_4(B\text{-}\beta\text{-}SbW_9O_{33})_2]^{6-}$ and $\{[Ln(H_2O)_8]_2[Fe_4W_2O_7(H_2O)_4(pic)_2(Hpic)_2(B\text{-}\beta\text{-}SbW_9O_{33})_2]\}^{4-}$ moieties. The molecular units of **8**−**9** contain two identical quadripic-inserted Krebs-type $\{[Ln(H_2O)_6]_2[Fe_4(H_2O)_2(Hpic)_2(pic)_2(B\text{-}\beta\text{-}SbW_9O_{33})_2]\}^{2-}$ moieties, and both display a 1-D heterometallic double chain. For all we know, **1**−**9** stand for the first 3d−4f heterometallic tungstoantimonate hybrids functionalized by pic ligands. Particularly, the solid-state NIR photoluminescence (PL) spectrum in the range of 800−1450 nm of **3** and the solid-state visible PL spectra in the range of 500−750 nm of **4**, **5**, **7**, and **8** at room temperature display the featured fluorescence emission bands stemming from Ln^{3+} cations. In the PL emission procedures of **5** and **7**, energy transfer from $[B\text{-}\beta\text{-}SbW_9O_{33}]^{9-}$ fragments and pic ligands to Ln^{3+} ions has been observed. Additionally, the correlated color temperatures of **4**, **5**, **7**, and **8** are indexed to 2731, 2020, 4557, and 1685 K, respectively.

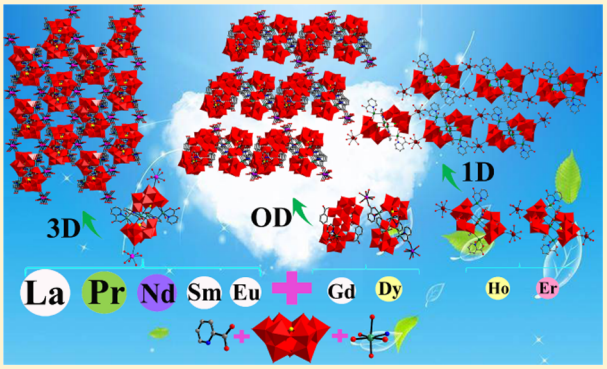

INTRODUCTION

Organic−inorganic hybrid materials (OIHMs) have intensively appealed to increasingly significant research enthusiasm over the last few decades not only because of their multitudinous chemical compositions and versatile binding modes in complicated structures but also because of the delicately synergetic effects between organic and inorganic ingredients creating extraordinary and available phenomena in fundamental and practical fields such as catalysis, magnetism, and photoelectricity.[1−10] Polyoxometalates (POMs), representing a particular class of charming metal-oxo clusters constructed from early transition metals with enormously diversified topologies, fascinating performances, and practical potentials in the various domains of catalysis, medicine, magnetism, optics, electrochemistry, sorption, and materials science,[11−22] can function as preeminent inorganic polydentate ligands to combine with diverse 3d- or 4f-metal cations constructing novel functional hybrid materials resulting from their controllable physicochemical functionalities at the micro scale and cooperative interactions within POMs and extraneous metal ions. Interestingly, in the field of POM chemistry, a hot area of research is the design and synthesis of innovative POM-based OIHMs (POMOIHMs) with specific functionalities. Fundamentally, the elaborate choice of appropriate POM building blocks is significant for fabricating diverse POMOIHMs. Hence, the classical trilacunary Keggin POM segments with the high reactivity, considerable structural diversity, and coordination flexibility have been opted and some representative POM precursors *consist* of (i) trilacunary Keggin segments containing

Received: July 25, 2018
Published: November 27, 2018

DOI: 10.1021/acs.inorgchem.8b02103
Inorg. Chem. 2018, 57, 15079−15092

lone-pair electrons [A-α-XW_9O_{33}]$^{8/9-}$, [A-β-XW_9O_{33}]$^{8/9-}$, [B-α-XW_9O_{33}]$^{8/9-}$, and [B-β-XW_9O_{33}]$^{8/9-}$ (X = Te^{IV}, Se^{IV}, As^{III}, Sb^{III}, Bi^{III}) and (ii) trilacunary Keggin segments without lone-pair electrons [A-α-XW_9O_{34}]$^{9/10-}$, [A-β-XW_9O_{34}]$^{9/10-}$, [B-α-XW_9O_{34}]$^{9/10-}$, and [B-β-XW_9O_{34}]$^{9/10-}$ (X = P^V, As^V, Si^{IV}, Ge^{IV}). By introducing some available 3d-metal complexes as connectors or ornaments to inorganic POM matrixes, a great deal of 3d-metal-substituted POMOIHMs were acquired.[23−25] On the other hand, some 4f-metal-containing POMOIHMs were also obtained.[26−30] However, the continuous research on novel 3d−4f heterometallic (DFH) POMOIHMs was relatively less developed. Even so, some DFH POMOIHMs have been already achieved. For example, in 2011, Reinoso et al. prepared an antiferromagnetic Cu−Ce heterometallic POM-based hybrid [{Ce(OAc)} $Cu_3(H_2O)$(B-α-$GeW_9O_{34})_2$]$^{11-}$ comprising an unprecedented tricopper-substituted and {Ce(OAc)}$^{3+}$-incorporated Weakley-type germanotungstate unit by using a step-by-step reaction.[31] By mixing [A-α-$HAsW_9O_{34}$]$^{8-}$, Cu^{2+}, Ln^{3+}, and en, a class of 2-D DFH arsenotungstate hybrids [$Cu(en)_2$ (H_2O)][$Cu(en)_2$]$_{1.5}$[Ln(α-$AsW_{11}O_{39})_2$]$^{6-}$ (Ln^{3+} = Pr^{3+}, Nd^{3+}, Sm^{3+}, Eu^{3+}, Tb^{3+}) were made by our lab in 2012.[32] Yang's team hydrothermally obtained an organic−inorganic hybrid 3-D DFH hybrid [$Ce_2(ox)_3(H_2O)_2$]$_2$ {[Mn-$(H_2O)_3$]$_2$[$Mn_4(GeW_9O_{34})_2(H_2O)_2$]}$^{8-}$ constructed from quadriMn-sandwiched germanotungstates via 3d- and 4f-metal bridges in 2013.[33] As far as we know, reports on DFH tungstoantimonates (TAs) are extremely few. Apart from these purely inorganic DFH TAs,[34−36] only a group of organic−inorganic DFH TA hybrids [$Ln(H_2O)_8$]$_2$[Fe_4 $(H_2O)_8(thr)_2$][B-β-SbW_9O_{33}]$_2$·$22H_2O$ (Ln^{3+} = Pr^{3+}, Nd^{3+}, Sm^{3+}, Eu^{3+}) was first reported by us.[37]

With this background, as our continuous work of discovering novel DFH POMOIHMs,[37−39] the trilacunary [B-α-SbW_9O_{33}]$^{9-}$ {B-α-SbW_9} precursor was still selected as the polydentate candidate to capture 3d- or 4f-metal cations on account of vacant sites on the surface of its skeleton. It is worth mentioning that the Fe^{3+} ion possesses strong electrophilicity, which can offer the capacity of incorporating lacunary POMs together, resulting in the formation of Fe^{III}-substituted POM aggregates.[40−43] Additionally, N-heterocyclic aromatic carboxylic acid ligands with the rigid "pyridine spacer" have multifunctional oxygen and nitrogen coordinate sites, which tend to combine 3d- and/or 4f-metal ions and even W atoms together during the course of forming heterometallic POM-based materials. More importantly, compared with 3d-metal cations, 4f-metal ions possess the following features: (i) different coordinate geometry of 4f-metal ions may lead to various structures; (ii) 4f-metal ions own strong luminescence emissions and long decay lifetimes, thus, they usually serve to manufacture luminescent materials and laser medium;[44] and (iii) on the basis of the hard and soft acids and bases reaction rule,[45] 4f-metal ions are oxyphilic so that they could swimmingly combine with oxygenic ligands and serve as synergistic linkers to integrate POMs and organic ligands together, which may lead to extended structures. Herein, we report three types of pic-decorated DFH Keggin-type TAs: Na_4[$Ln(H_2O)_5$]$_2$[Fe_4 $(H_2O)_2(pic)_4$(B-β-$SbW_9O_{33})_2$]·$26H_2O$ [Ln^{3+} = La^{3+} (**1**), Pr^{3+} (**2**), Nd^{3+} (**3**), Sm^{3+} (**4**), Eu^{3+} (**5**)], Na_6H_4[$Fe_2W_4O_9(H_2O)_2(Hpic)_4$(B-$\beta$-$SbW_9O_{33})_2$] [$Ln(H_2O)_8$]$_2$[$Fe_4W_2$ $O_7(H_2O)_4(pic)_2(Hpic)_2$(B-$\beta$-$SbW_9O_{33})_2$]·$38H_2O$ [Ln^{3+} = Gd^{3+} (**6**), Dy^{3+} (**7**)], and Na_2H_2[{[$Ln(H_2O)_6$]$_2$[$Fe_4(H_2O)_2$ $(Hpic)_2(pic)_2$(B-β-$SbW_9O_{33})_2$]}$_2$·$44H_2O$ [Ln^{3+} = Ho^{3+} (**8**), Er^{3+} (**9**), Hpic = 2-picolinic acid]. The common structure characteristic of **1**−**5** encompasses a quadripic-inserted Krebs-type [$Fe_4(H_2O)_2(pic)_4$(B-β-$SbW_9O_{33})_2$]$^{10-}$ moiety supported by two hydrated [$Ln(H_2O)_5$]$^{3+}$ ions on both sides. Interestingly, quadripic-inserted [$Fe_4(H_2O)_2(pic)_4$(B-β-$SbW_9O_{33})_2$]$^{10-}$ moieties in **1**−**5** are further linked by the hydrated [$Ln(H_2O)_5$]$^{3+}$ cations and pic ligands, generating a 3-D extended heterometallic framework. **6**−**7** display an isolated structure and their striking characteristic is that their molecular units comprise two kinds of quadripic-inserted non-Krebs-type [$Fe_2W_4O_9(H_2O)_2(Hpic)_4$(B-$\beta$-$SbW_9O_{33})_2$]$^{6-}$ and {[Ln-$(H_2O)_8$]$_2$ [$Fe_4W_2O_7(H_2O)_4(pic)_2(Hpic)_2$(B-$\beta$-$SbW_9O_{33})_2$]}$^{4-}$ subunits. **8**−**9** shows the 1-D heterometallic double chain built by two crystallographically independent {[Ln-$(H_2O)_6$]$_2$[$Fe_4(H_2O)_2(Hpic)_2(pic)_2$(B-$\beta$-$SbW_9O_{33})_2$]}$^{2-}$ units through Ln^{3+} linkers. The structural discrepancies of **1**−**5**, **6**−**7**, and **8**−**9** may mainly stem from the synergistic effect between different coordinate geometries of the Ln^{3+} cations and various coordination modes of the Hpic ligand because their synthetic conditions are the same. To our knowledge, **1**−**9** are the first organic−inorganic DFH TA hybrids functionalized by pic ligands. Particularly, the photoluminescence (PL) performances of **3**, **4**, **5**, **7**, and **8** were studied at ambient temperature. Besides, **5** and **7** were utilized to explore the energy transfer from {B-β-SbW_9} fragments and pic components to Ln^{3+} ions and the results indicate that {B-β-SbW_9} fragments and pic components can sensitize the emission of Ln^{3+} ions. Furthermore, the color temperatures (CTs) of **4**, **5**, **7**, and **8** can be calculated as 2731, 2020, 4557, and 1685 K, respectively.

RESULTS AND DISCUSSION

Synthesis. **1**−**9** were prepared by reacting {B-α-SbW_9} and Fe^{3+} and Ln^{3+} ions in the presence of Hpic through mild hydrothermal synthesis method. On one hand, the hydrothermal technique has developed as an efficient approach to prepare novel hybrid materials because of its high pressure and temperature, which can efficiently increase the solubility of starting materials and reduce the viscosity of different components so as to promote their reaction activity and then to enhance the binding probabilities of diverse components.[46−52] As a result, the hydrothermal synthesis approach was selected. In addition, Hpic was introduced to our reaction system on account of the various binding manners and the assumption that high coordination capacity with diversified metal (3d- or/and 4f-metal) ions can give birth to novel DFH TAs. As expected, the 3d- and 4f-metal cations were both integrated into Hpic ligands in our reaction. On the synergistic effect between different coordination geometries of Ln^{3+} ions and various coordination modes of the Hpic ligand in the reaction process, three kinds of DFH TAs decorated by Hpic ligands were obtained, that is, the 3-D extended frameworks of **1**−**5**, the isolated structures of **6**−**7**, and the 1-D double chain of **8**−**9**. Obviously, the different coordination geometries of Ln^{3+} ions play a significant role in the structure variation of **1**−**9**. In **1**−**5** and **8**−**9**, Ln^{3+}ions respectively exhibit the eight-coordinate bicapped triangular prism and the eight-coordinate square antiprism, whereas the Ln^{3+} ions in **6**−**7** adopt the nine-coordinate tricapped triangular prism (vide infra). Furthermore, the various binding manners of Hpic ligands also contribute to the formation of **1**−**9** (vide infra). The binding modes of Hpic ligands with various metal cations in this paper are demonstrated in Figure 1. The Krebs-type TAs can be described as follows: two {WO_2} groups are combined with two {B-β-SbW_9} fragments to form a bisdecatungstate [$Sb_2W_{20}O_{70}$]$^{14-}$, which is further

DOI: 10.1021/acs.inorgchem.8b02103
Inorg. Chem. 2018, 57, 15079−15092

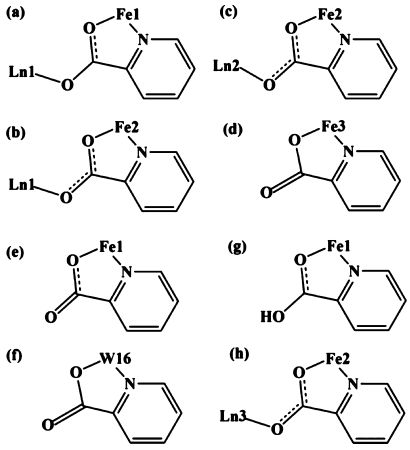

Figure 1. (a,b) Binding modes of pic ligands observed in **1**−**5**. (c−f) Coordination modes of pic ligands observed in **6**−**7**. $Ln1^{3+}$ = La^{3+}, Pr^{3+}, Nd^{3+}, Sm^{3+}, Eu^{3+}; $Ln2^{3+}$ = Gd^{3+}, Dy^{3+}; (g,h) Coordination modes of pic ligands observed in **8**−**9**. $Ln3^{3+}$ = Ho^{3+}, Er^{3+}.

stabilized by the addition of two *fac*-WO_3 or two $\{M^{n+}(H_2O)_3\}$ ions, which provides an excellent possibility for forming various 3d-metal-inserted Krebs-type derivatives. Because the tetra-Fe^{III}-inserted Krebs-type $[Fe_4(H_2O)_{10}(B\text{-}\beta\text{-}SbW_9O_{33})_2]^{10-}$ unit contains ten labile aqua ligands on Fe^{3+} ions (Figure 2a), based on the synthetic concept that organic ligands can substitute the labile aqua ligands on Fe^{3+} ions, several quadri-Fe^{III}-inserted Krebs-type TA hybrids have been discovered (Figure 2b,c). Apparently, eight labile aqua ligands on the iron centers can be replaced by four oxalate (ox) ligands in $[Fe_4(ox)_4(B\text{-}\beta\text{-}SbW_9O_{33})_2]^{14-}$ (Figure 2b), forming the ox-functionalized 1-D extended chain,[42] whereas two threonine (thr) ligands replaced two labile waters on the iron centers in $[Ln(H_2O)_8]_2[Fe_4(H_2O)_8(thr)_2][B\text{-}\beta\text{-}SbW_9O_{33}]_2\cdot 22H_2O$ (Ln^{3+} = Pr^{3+}, Nd^{3+}, Sm^{3+}, Eu^{3+}) (Figure 2c).[37] Additionally, the structures of **1**−**5** and **8**−**9** in this paper also show an octa-substituted mode (Figure 2d,e). Fascinatingly, we can find that flexible ox and thr ligands tend to construct the low-dimensional structures, whereas rigid Hpic ligand can favor the creation of extended frameworks. Specifically, the ox-substituted Krebs-type unit can come into a 1-D chain (Figure 2f), the thr-substituted Krebs-type unit remains an isolated structure (Figure 2g), and the pic-substituted Krebs-type unit can result

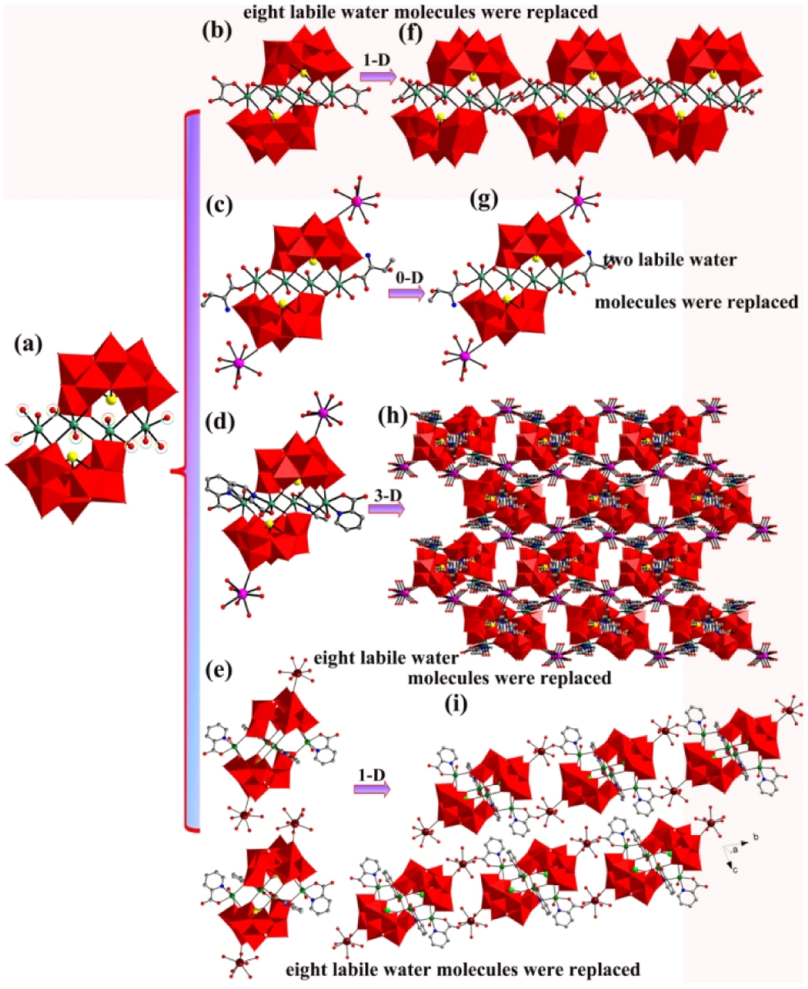

Figure 2. (a) View of the quadriFe^{III}-inserted Krebs-type $[Fe_4(H_2O)_{10}(B\text{-}\beta\text{-}SbW_9O_{33})_2]^{10-}$ unit. (b) View of the ox-substituted Krebs-type $[Fe_4(ox)_4(B\text{-}\beta\text{-}SbW_9O_{33})_2]^{14-}$ unit. (c) View of the thr-substituted structure of $[Ln(H_2O)_8]_2[Fe_4(H_2O)_8(thr)_2][B\text{-}\beta\text{-}SbW_9O_{33}]_2\cdot 22H_2O$. (d) View of the pic-substituted Krebs-type unit observed in **1**−**5** in this paper. (e) View of the pic-substituted Krebs-type unit observed in **8**−**9** in this paper. (f) One-D chain formed by ox-substituted Krebs-type units. (g) thr-substituted isolated structure. (h) Three-D extended framework observed in **1**−**5** in this paper. (i) One-D double chain observed in **8**−**9** in this paper.

DOI: 10.1021/acs.inorgchem.8b02103
Inorg. Chem. 2018, 57, 15079−15092

in a 3-D extended framework (Figure 2h) and 1-D double chain (Figure 2i).

Unlike the structures of **1**−**5** and **8**−**9**, the common feature of **6** and **7** is that they contain two different DFH non-Krebs-type polyoxoanions $[Fe_2W_4O_9(H_2O)_2(Hpic)_4(B\text{-}\beta\text{-}SbW_9O_{33})_2]^{6-}$ and $\{[Ln(H_2O)_8]_2[Fe_4W_2O_7(H_2O)_4(pic)_2(Hpic)_2(B\text{-}\beta\text{-}SbW_9O_{33})_2]\}^{4-}$ subunits. It is worthwhile that the phenomenon that pic ligands are combined with W atoms is very infrequent.[30,53,54] During the course of our exploration, we noticed that the pH variation also played an indispensable part in the synthesis of **1**−**9**. Paralleling experimental investigations indicate that the final pH value of 1.0−1.4 is helpful for the formation of **1**−**9** and has optimum yields. However, with the pH value beyond this range, keeping other reaction conditions unchanged, amorphous precipitates were formed at the end of the reaction. Another interesting phenomenon is the different coordination geometries of the Ln^{3+} cations. When La^{3+}, Pr^{3+}, Nd^{3+}, Sm^{3+}, and Eu^{3+}cations were used, the 3-D frameworks of **1**−**5** were obtained. Nevertheless, the use of Gd^{3+} and Dy^{3+} cations gave rise to the isolated structures of **6**−**7**. Beyond expectation, when employing the Ho^{3+} and Er^{3+} cations, the 1-D double chain is created.

Structure Description. The measured powder X-ray diffraction (PXRD) spectra of **3**, **4**, **5**, **7**, and **8** coincide with their simulative XRD spectra based on the X-ray structural analysis, indicating that all of the samples are pure (Figure S1).

The molecular structural units of isostructural **1**−**5** (space group $P2(1)/n$) include a quadriFe^{III}-inserted Krebs-type $[Fe_4(H_2O)_2(pic)_4(B\text{-}\beta\text{-}SbW_9O_{33})_2]^{10-}$ moiety supported by two $[Ln(H_2O)_5]^{3+}$ pendants on both terminals. Hence, only the structure discussion of **2** is exemplified. The structure segment of **2** embraces a quadripic-inserted $[Pr(H_2O)_5]_2[Fe_4(H_2O)_2(pic)_4(B\text{-}\beta\text{-}SbW_9O_{33})_2]^{4-}$ hybrid subunit, four Na^+ ions, and 26 crystal waters (Figure 3a). The Krebs-type $[Pr(H_2O)_5]_2[Fe_4(H_2O)_2(pic)_4(B\text{-}\beta\text{-}SbW_9O_{33})_2]^{4-}$ subunit encapsulates a tetraFe^{III} $\{Fe_4(H_2O)_2(pic)_4\}$ group (Figure 3b), in which four Fe^{3+} ions are situated on four vertexes of a rhomb with two neighboring edges of 5.613 and 5.566 Å. In the sandwich belt, adjacent tetraFe^{3+} ions are combined via the Fe−O−W−O−Fe linkages and the Fe2···Fe2A separation is 5.330 Å, whereas the distance of two external Fe1···Fe1A ions is 9.827 Å (Figure S2). In addition, the sandwich belt is constituted by two kinds of nonequivalent Fe^{3+} ions (two internal $Fe2^{3+}$ ions and two external $Fe1^{3+}$ ions). Albeit both inequivalent Fe^{3+} ions exhibit octahedral configurations, both binding environments are slightly disparate. The octahedron of the $Fe1^{3+}$ ion (Figure 3c) is constructed from two O atoms (O33, O38) of a {B-β-SbW_9} [Fe−O: 1.921(7)−1.950(7) Å], one O atom (O10A) of another {B-β-SbW_9} [Fe−O: 1.975(7) Å], one water O atom (O1W) [Fe−O: 2.097(8) Å], one carboxylic O atom (O2), and one N atom (N1) root in pic [Fe−O: 2.055(7) Å, Fe−N: 2.148(9) Å]. Besides, O38 and O1W atoms occupy the polar positions of the octahedral $Fe1^{3+}$, whereas O2, O10A, O33, and N1 atoms take up the equatorial plane. Interestingly, in **2**, the dihedral angle between the plane containing two W5 atoms and two Fe2 ions and the plane containing four Fe^{3+} ions is 132.21(20)° (Figure S3). Analogously, the octahedral $Fe2^{3+}$ ion (Figure 3d) is built by two O atoms (O4A, O5A) of one {B-β-SbW_9} [Fe−O: 1.937(6)−1.959(7) Å], two O atoms (O7, O16) of the other {B-β-SbW_9} [Fe−O: 1.958(7)−1.944(6) Å], one carboxylic O atom (O18), and the N atom (N2) of pic [Fe−O: 2.091(7) Å, Fe−N: 2.167(9) Å]. Furthermore, O5A and O18 atoms sit on the polar sites of the octahedral $Fe2^{3+}$ cation and

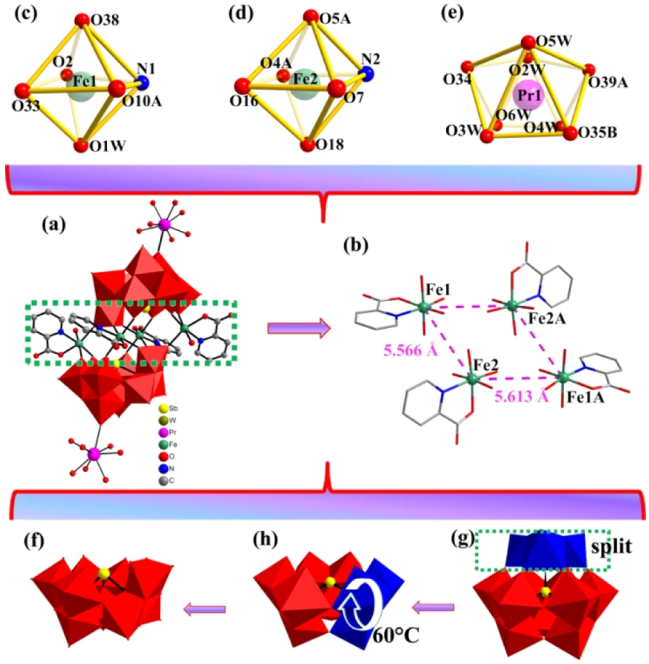

Figure 3. (a) Structure fragment of **2**. (b) $\{Fe_4(H_2O)_2(pic)_4\}$ group. (c,d) Octahedral geometries of $Fe1^{3+}$ and $Fe2^{3+}$ ions. (e) Twisted bicapped triangular prism of the $Pr1^{3+}$ cation. (f) $[B\text{-}\beta\text{-}SbW_9O_{33}]^{9-}$ segment. (g) Hypothetical parent α-Keggin $[\alpha\text{-}SbW_{12}O_{40}]^{5-}$ polyoxoanion. (h) $[B\text{-}\alpha\text{-}SbW_9O_{33}]^{9-}$ segment. N: blue, O: red, C: dark gray, Pr: pink, Sb: yellow, W: dark yellow, and $\{WO_6\}$: red. Symmetry codes: A: $2-x, -y, -1-z$. B: $-0.5+x, -0.5-y, 0.5+z$.

O4A, O7, O16, and N2 atoms establish the equatorial plane. It is interesting that two coordinated water ligands on each Fe^{3+} cation are replaced by one carboxylic O atom and one N atom from a pic ligand (Figure S4). To our knowledge, this phenomenon that four pic ligands simultaneously substitute eight coordinate water ligands located at the Krebs-type polyoxoanion is observed for the first time. The disordered $Pr1^{3+}$ ion is distributed over two sites with the occupation ratio of 75 and 25% and links to a terminal O atom of a {B-β-SbW_9}. The $Pr1^{3+}$ ion inhabits in a distorted bicapped triangular prism, which is established by a terminal O34 atom of a {B-β-SbW_9} [Pr−O: 2.448(7) Å], two carboxyl O atoms (O35B, O39A) of two pic groups [Pr−O: 2.379(8)−2.521(9) Å], and five aqueous ligands (O2W, O3W, O4W, O5W, and O6W) [Pr−O: 2.423(18)−2.561(12) Å] (Figure 3e). The {B-β-SbW_9} (Figure 3f) fragment could be deemed to originate from the hypothetical parent α-Keggin $[\alpha\text{-}SbW_{12}O_{40}]^{5-}$ polyoxoanion (Figure 3g) by taking away one $\{W_3O_{13}\}$ trimer group to form the {B-α-SbW_9} segment (Figure 3h) and accompanying 60° clockwise rotation of one $\{W_3O_{13}\}$ trimer among the remaining three $\{W_3O_{13}\}$ trimers. Notably, the starting material is {B-α-SbW_9}, therefore, it is clear that the {B-α-SbW_9} segment in the precursor must have isomerized to the {B-β-SbW_9} segment in the products, which has been previously encountered.[55−67]

Notably, adjacent structural units are connected to generate the 1-D chain by the coordination of $Pr1^{3+}$ ions with O atoms on the pic ligands that chelate to the exterior $Fe1^{3+}$ cations (Figure 4a,b). Ulteriorly, the 1-D chains are interlinked via the coordination of $Pr1^{3+}$ ions with O atoms on the pic ligands that chelate to the internal $Fe2^{3+}$ ions to create a 2-D layer (Figure 4c,d). Finally, adjacent layers are also interconnected by $Pr1^{3+}$ ions with O atoms on the pic ligands that chelate to the

DOI: 10.1021/acs.inorgchem.8b02103
Inorg. Chem. 2018, 57, 15079−15092

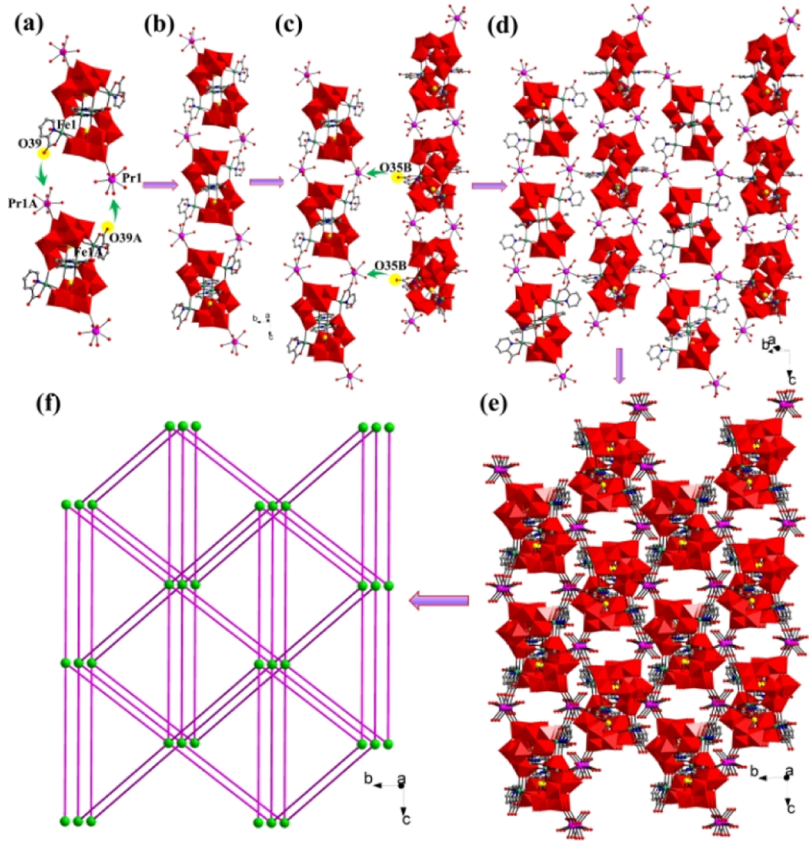

Figure 4. (a,b) Adjacent molecular structural units are linked to give rise to the 1-D chain by Pr^{3+} cations and pic ligands that chelate to the exterior $Fe1^{3+}$ ions. (c,d) Adjacent 1-D chains are interlinked to create the 2-D layer structure via pic ligands that coordinate to the internal $Fe2^{3+}$ and Pr^{3+} ions. (e) Adjacent 2-D layers are also interlaced to create the 3-D extended structure via pic ligands that coordinate to the internal $Fe2^{3+}$ and Pr^{3+} ions. (f) Three-D framework topology. N: blue, O: red, C: dark gray, Pr: pink, Sb: yellow, W: dark yellow, and $\{WO_6\}$: red. Symmetry codes: A: $2 - x, -y, -1 - z$. B: $-0.5 + x, -0.5 - y, 0.5 + z$.

internal $Fe2^{3+}$ ions and construct a 3-D extended framework (Figure 4e). By considering the molecular structural unit of **2** as a six-connected node, the 3-D framework can be understood as a 3-D topological network with Schläfli symbol of $(4^6{\cdot}6^6)$ (Figures 4f and S5). For all we know, **2** represents the first 3-D extended framework fabricated by the quadripic-inserted Krebs-type units through Pr^{3+} and pic linkers.

Nevertheless, the molecules of **6**−**7** (space group $P\bar{1}$) comprise two kinds of quadripic-inserted non-Krebs-type $[Fe_2W_4O_9(H_2O)_2(Hpic)_4(B\text{-}\beta\text{-}SbW_9O_{33})_2]^{6-}$ and $\{[Ln(H_2O)_8]_2[Fe_4W_2O_7(H_2O)_4(pic)_2(Hpic)_2(B\text{-}\beta\text{-}SbW_9O_{33})_2]\}^{4-}$ moieties. However, only **7** is discussed herein. The structure of **7** contains a quadripic-inserted non-Krebs-type $[Fe_2W_4O_9(H_2O)_2(Hpic)_4(B\text{-}\beta\text{-}SbW_9O_{33})_2]^{6-}$ (**c**) moiety, a quadripic-inserted non-Krebs-type $\{[Dy(H_2O)_8]_2[Fe_4W_2O_7(H_2O)_4(pic)_2(Hpic)_2(B\text{-}\beta\text{-}SbW_9O_{33})_2]\}^{4-}$ (**d**) moiety, six Na^+ ions, four protons, and 38 lattice water molecules (Figure 5a). The sandwich-type **c** moiety (Figures 5b and S6a) is made up of two $\{B\text{-}\beta\text{-}SbW_9\}$ (Figure 5c) fragments encapsulating an unprecedented organic−inorganic hybrid quadripic-inserted hexa-nuclear heterometallic $\{Fe_2W_4O_9(H_2O)_2(Hpic)_4\}$ group (Figure 5d). In the $\{Fe_2W_4O_9(H_2O)_2(Hpic)_4\}$ group, Fe1, Fe1B, W16, and W16B atoms are aligned in a rectangle with the Fe1···W16B distance of 5.099 Å and the Fe1···W16 distance of 7.100 Å. W10 and W10B are inside the rectangle and bridge Fe1, Fe1B, W16, and W16B together via four oxygen atoms, and W10 and W10B are joined to each other through one oxygen atom. The W10···W10B distance is 3.884 Å. Interestingly, two Hpic ligands coordinate to W16 and W16B, whereas two Hpic ligands coordinate to Fe1 and Fe1B. In addition, the Fe1···Fe1B and W16···W16B distances are 8.844 and 8.639 Å, respectively (Figure S7). The sandwich-type **d** moiety (Figures 5e and S6b) is also constituted by two $\{B\text{-}\beta\text{-}SbW_9\}$ segments (Figure 5f) connected by an interesting organic−inorganic hybrid quadripic-inserted octa-nuclear heterometallic $\{[Dy(H_2O)_8]_2[Fe_4W_2O_7(H_2O)_4(pic)_2(Hpic)_2\}$ group (Figure 5g). In the $\{[Dy(H_2O)_8]_2[Fe_4W_2O_7(H_2O)_4(pic)_2(Hpic)_2\}$ group, Fe2, Fe3, Fe2A, and Fe3A atoms constitute a rectangle with the Fe2···Fe3 distance of 5.201 Å and the Fe2···Fe3A distance of 7.034 Å. The Fe3 and Fe3A distance is 8.757 Å, and the Fe2 and Fe2A distance is 8.739 Å (Figure S8). Each Fe^{3+} is coordinated by a pic ligand. W24 and W24A join Fe2, Fe3, Fe2A, and Fe3A together through four O atoms, and W24 and W24A are integrated via one oxygen atom. The W24 and W24A distance is 4.670 Å. Above all, $[Dy1(H_2O)_8]^{3+}$ and $[Dy1A(H_2O)_8]^{3+}$ ions, respectively, graft to Fe2 and Fe2A ions through the bridging function of the pic ligand. As far as we know, such quadripic-inserted octa-nuclear heterometallic $\{[Dy(H_2O)_8]_2[Fe_4W_2O_7(H_2O)_4(pic)_2(Hpic)_2\}$ group is encountered for the first time in POM chemistry. It should be pointed out that the most conspicuous difference between **c** and **d** units lies in their sandwich cores; the sandwich core in the **c** unit includes a quadripic-inserted hexa-nuclear heterometallic $\{Fe_2W_4O_9(H_2O)_2(Hpic)_4\}$ group, whereas the sandwich core in the **d** unit is a quadripic-inserted octa-nuclear heterometallic

DOI: 10.1021/acs.inorgchem.8b02103
Inorg. Chem. 2018, 57, 15079−15092

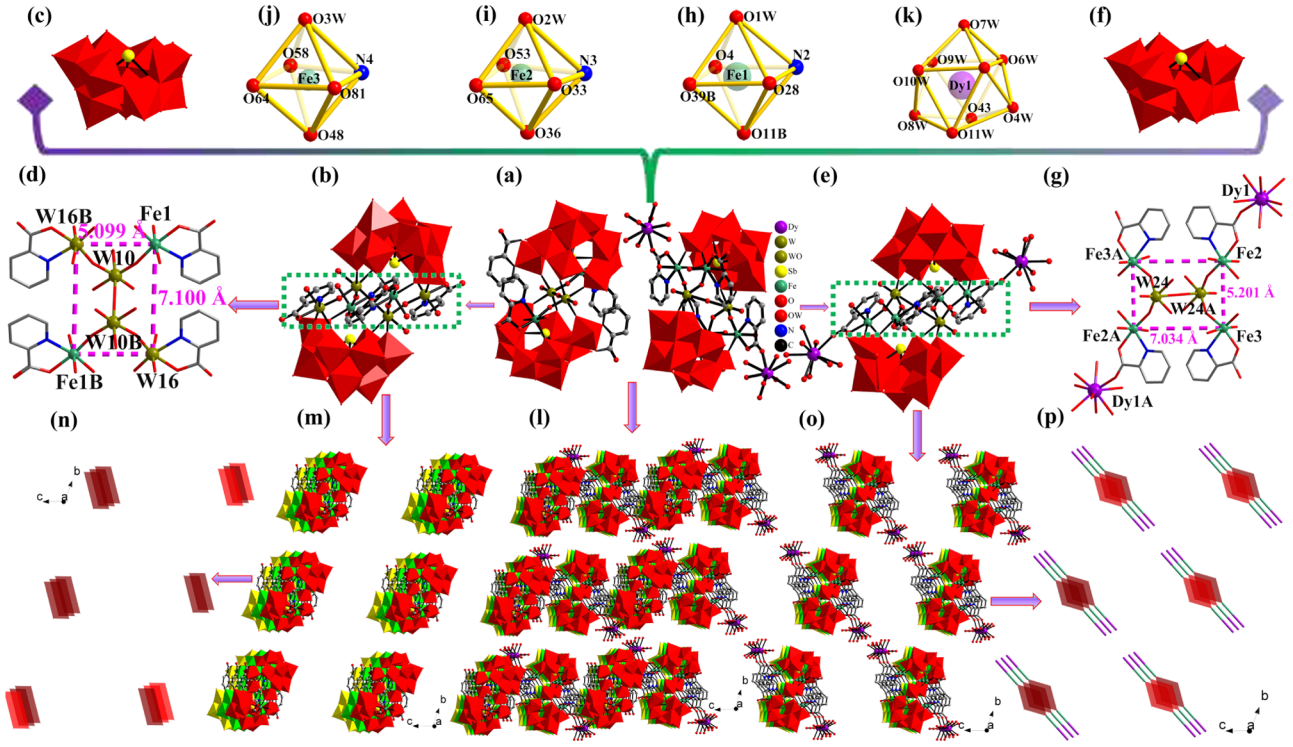

Figure 5. (a) Molecular unit of **7**. (b) The structure of **c**. (c) {B-β-SbW_9} fragment in **c**. (d) Tetra-pic-substituted hexa-nuclear heterometallic $\{Fe_2W_4O_9(H_2O)_2(Hpic)_4\}$ group in the sandwich-belt of **c** highlighting the distances of Fe1···W16B and Fe1B···W16B. (e) Structure of **d**. (f) {B-β-SbW_9} fragment in **d**. (g) Octa-nuclear heterometallic $\{[Dy(H_2O)_8]_2[Fe_4W_2O_7(H_2O)_4(pic)_2(Hpic)_2\}$ group highlighting the distances of Fe2···Fe3 and Fe2···Fe3A. (h,k) Coordination environments of $Fe1^{3+}$, $Fe2^{3+}$, $Fe3^{3+}$, and $Dy1^{3+}$ ions in **7**. (l) Stacking alignment of **7** viewed along the *a* axis. (m,n) Packing alignment and simplified scheme of **c** in **7** along the *a* axis. (o,p) Packing alignment and simplified scheme of **d** in **7** along the *a* axis. N: blue, O: red, C: dark gray, Dy: purple, Sb: yellow, W: dark yellow, and $\{WO_6\}$: red. Symmetry codes: A: $2-x, 3-y, 1-z$. B: $3-x, 3-y, 2-z$.

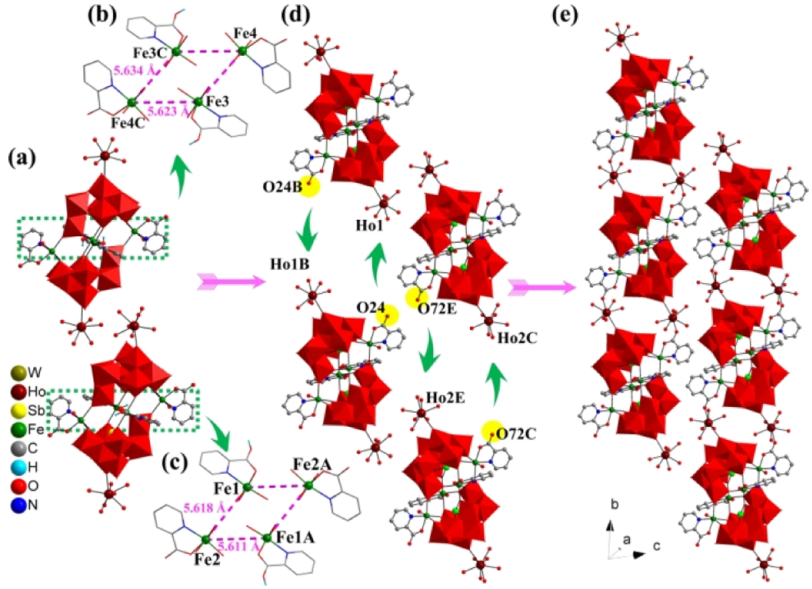

Figure 6. (a) Structural unit of **8**. (b,c) $\{Fe_4(H_2O)_2(Hpic)_2(pic)_2\}$ groups in **8**. (d,e) Adjacent molecular structural units linked by Ho^{3+} cations and pic ligands that chelate to the exterior Fe^{3+} cations to form the 1-D double chain. N: blue, O: red, C: dark gray, H: sky blue, Ho: dark red, Sb: yellow, W: dark yellow, and $\{WO_6\}$: red.

$\{[Dy(H_2O)_8]_2[Fe_4W_2O_7(H_2O)_4(pic)_2(Hpic)_2\}$ group. Overtly, there are three types of crystallographically unique Fe^{3+} ions in **7**, namely, $Fe1^{3+}$ cation in the **c** unit and $Fe2^{3+}$ and $Fe3^{3+}$ ions in the **d** unit. Albeit the three Fe^{3+} ions exhibit the distorted octahedral configurations, their binding environments are distinguishing. The octahedron of the $Fe1^{3+}$ ion (Figure 5h) is established by two O atoms (O11B, O39B) of one {B-β-SbW_9} [Fe−O: 1.95(2)−1.984(18) Å], one O atom (O4) of another {B-β-SbW_9} [Fe−O: 1.908(16) Å], one aqueous ligand (O1W) [Fe−O: 2.06(2) Å], one carboxylic O atom (O28), and one N (N2) atom of a pic [Fe−O: 2.03(2) Å, Fe−N: 2.19(2) Å]. Similarly, the octahedral $Fe2^{3+}$ ion (Figure 5i) is built by two O atoms

DOI: 10.1021/acs.inorgchem.8b02103
Inorg. Chem. 2018, 57, 15079−15092

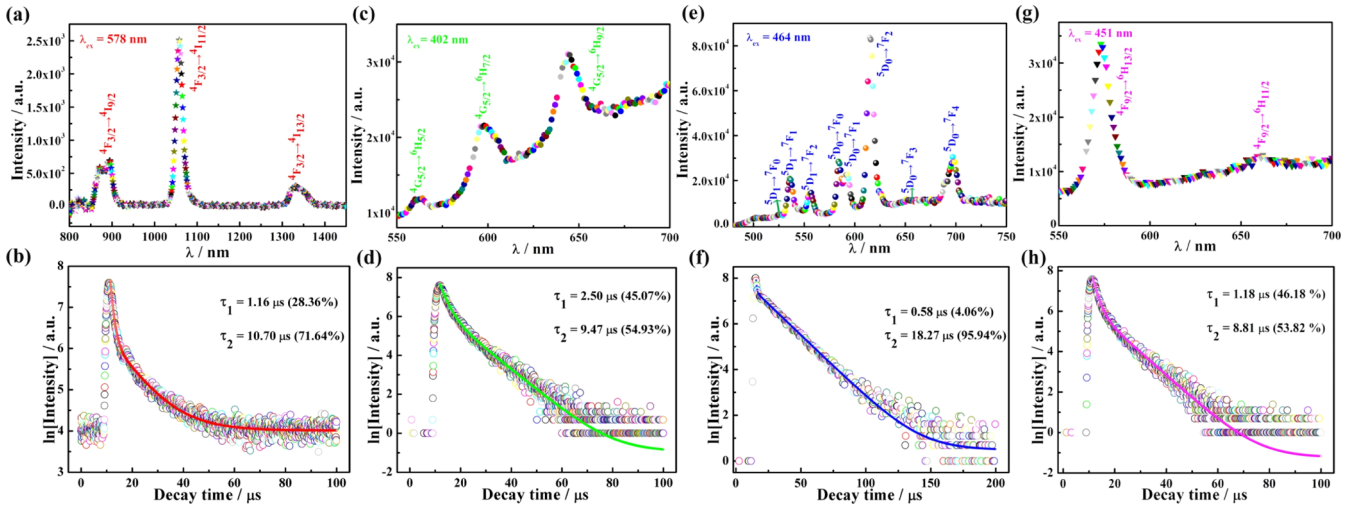

Figure 7. (a) Solid-state emission spectrum of **3** (λ_{ex} = 584 nm) at room temperature. (b) Luminescence decay curve of **3** taken by monitoring the emission at 1059 nm. (c) Solid-state emission spectrum of **4** (λ_{ex} = 402 nm) at room temperature. (d) Luminescence decay curve of **4** taken by monitoring the emission at 644 nm. (e) Solid-state emission spectrum of **5** (λ_{ex} = 464 nm) at room temperature. (f) Luminescence decay curve of **5** taken by monitoring the emission at 617 nm. (g) Solid-state emission spectrum of **7** (λ_{ex} = 451 nm) at room temperature. (h) Luminescence decay curve of **7** taken by monitoring the emission at 575 nm.

(O36, O65) of one {B-β-SbW_9} [Fe−O: 1.92(2)−1.99(2) Å], one O atom (O33) of the other {B-β-SbW_9} [Fe−O: 1.94(2) Å], one water molecule (O2W) [Fe−O: 2.11(2) Å], one carboxylic O atom (O53), and a N atom (N3) of a pic [Fe−O: 2.07(2) Å, Fe−N: 2.11(2) Å]. Moreover, the octahedral geometry of the $Fe3^{3+}$ cation (Figure 5j) is identical to those of $Fe1^{3+}$ and $Fe2^{3+}$ cations and is constituted by two O atoms (O48, O64) of one {B-β-SbW_9} [Fe−O: 1.84(3)−2.04(3) Å], one O atom (O58) from the other {B-β-SbW_9} [Fe−O: 1.91(2) Å], one coordinate water molecule (O3W) [Fe−O: 1.89(3) Å], one carboxylic O atom (O81), and one N atom (N4) of a pic [Fe−O: 2.02(3) Å, Fe−N: 2.32(3) Å]. Furthermore, the polar positions of octahedral $Fe1^{3+}$, $Fe2^{3+}$, and $Fe3^{3+}$ cations are occupied by O11B, O1W; O36, O2W; and O48, O3W, respectively. Their equatorial planes are constituted by O4, O28, O39B, N2; O33, O53, O65, N3; and O58, O64, O81, N4, respectively. Additionally, the $Dy1^{3+}$ cation directly coordinates to the carboxylate oxygen of the pic. The $Dy1^{3+}$ ion grafting to the sandwich belt adopts a twisted tricapped triangular prism configuration formed by an O atom (O43) of a pic [Dy−O: 2.29(2) Å] and eight water ligands (O4W, O5W, O6W, O7W, O8W, O9W, O10W, and O11W) [Dy−O: 2.33(3)−2.53(3) Å] (Figure 5k). More importantly, the molecular units $\{[Fe_2W_4O_9(H_2O)_2(Hpic)_4(B\text{-}\beta\text{-}SbW_9O_{33})_2][Dy(H_2O)_8]_2[Fe_4W_2O_7(H_2O)_4(pic)_2(Hpic)_2(B\text{-}\beta\text{-}SbW_9O_{33})_2]\}^{10-}$ are trimly distributed in the −AAA− fashion in the *bc* plane (Figures 5l and S9). The stacking alignments and simplified packing representations of **c** and **d** units in the *bc* plane are exhibited in Figure 5m−p.

8−**9** are isomorphous and only **8** is described here. The structural unit of **8** includes two identical quadriFe^{III}-sandwiched Krebs-type subunits $\{[Ho(H_2O)_6]_2[Fe_4(H_2O)_2(Hpic)_2(pic)_2(B\text{-}\beta\text{-}SbW_9O_{33})_2]\}^{2-}$ (Figure 6a). Notably, the quadriFe^{III}-sandwiched Krebs-type subunits in **8** are similar to those in **2**. Each of the Krebs-type $\{[Ho(H_2O)_6]_2[Fe_4(H_2O)_2(Hpic)_2(pic)_2(B\text{-}\beta\text{-}SbW_9O_{33})_2]\}^{2-}$ subunits in **8** also consists of quadriFe^{III} $\{Fe_4(H_2O)_2(Hpic)_2(pic)_2\}$ groups (Figure 6b,c), and the distances between Fe^{3+} ions are as follows: Fe3···Fe4C is 5.623 Å, Fe3C···Fe4C is 5.634 Å, Fe1···Fe2 is 5.618 Å, and Fe1A···Fe2 is 5.611 Å. The distances of Fe1···Fe1A and Fe3···Fe3C are 9.827 and 5.33 Å, respectively, whereas the distances of Fe2···Fe2A and Fe4···Fe4C are 9.88 and 9.91 Å, respectively (Figure S10). Each of the tetra-Fe^{III} $\{\{Fe_4(H_2O)_2(Hpic)_2(pic)_2\}$ groups in **8** is also defined by two kinds of inequivalent Fe^{3+} ions. Although all Fe^{3+} ions in **8** display the hexa-coordinate geometries, their chemical environments are diverse (Figure S11a−d). Moreover, the dihedral angles between the surface containing two W and two Fe centers and the surface containing four Fe^{3+} ions in two quadriFe^{III}-sandwiched Krebs-type subunits in **8** are 133.03(29)° and 133.18 (30)° (Figure S12). The $Ho1^{3+}$ and $Ho2^{3+}$ cations inhabit an eight-coordinate distorted square antiprism configuration (Figure S11e,f). Apparently, adjacent molecular structural units are connected by the coordination of $Ho1^{3+}$ and $Ho2^{3+}$ ions with O (O24, O24B, O72C, and O72E) atoms on the pic ligands that chelate to the exterior Fe^{3+} ions, producing the 1-D double chain (Figure 6d,e). However, the pic ligands chelated to the interior Fe^{3+} cations are protonated, so that they cannot connect to the Ho^{3+} ions to create a network structure.

Of particular concern is that **2**, **7**, and **8** have some differences, albeit they are somewhat similar (Figure S13a−c). First, the polyoxoanion units of **2**, **7**, and **8** could be considered as dimeric units of trilacunary {B-β-SbW_9} fragments. Second, the coordination number and coordination geometry of Ln^{3+} cations in **2**, **7**, and **8** are different. In **2** and **8**, Pr^{3+} and Ho^{3+} ions, respectively, exhibit the octa-coordinate bicapped triangular prism and the octa-coordinate square antiprism, whereas the Dy^{3+} ion in **7** adopts a nona-coordinate tricapped triangular prism (Figure S13d−f). Third, the sandwich-belt cores in **2**, **7**, and **8** are completely distinct. In **2** and **8**, the sandwich-belt cores are the quadripic-inserted tetra-nuclear iron centers, whereas the sandwich-belts in **7** display the quadripic-inserted octa-nuclear heterometallic group and the quadripic-inserted hexa-nuclear heterometallic group (Figure S13g−j). More importantly, **2** evolves into an unrivalled 3-D framework via Pr^{3+} and pic linkers (Figure S13k), **8** evolves into the 1-D

DOI: 10.1021/acs.inorgchem.8b02103
Inorg. Chem. 2018, 57, 15079−15092

double chain via Ho^{3+} and pic linkers (Figure S13l), whereas **7** is an isolated structure with two types of non-Krebs-type quadripic-inserted polyoxoanions (Figure S13m).

PL Properties. In recent years, the unusual electronic properties of the trivalent Ln ions make them well used as luminescent groups with many currently developing applications in the optical field.[58] Ln-based luminescence complexes play an indispensable role in developing novel optical materials because of their merits, such as high quantum yield, narrow bandwidth, and so forth.[58−60] It can be easily interpreted by electronic configuration of Ln ions. Moreover, the 4f orbitals shielded by the $5s^25p^6$ subshells bring about specific spectroscopic properties, such as parity-forbidden f−f absorptions having fairly low molar absorption coefficients (generally <10 M^{-1} cm^{-1}) and the characteristic sharp linelike emission peaks, prevailingly in the visible and NIR region.[61] In this context, the solid-state PL properties of **3**, **4**, **5**, **7**, and **8** at room temperature were investigated.

On excitation at 584 nm, the NIR PL spectrogram of **3** (Figure 7a) demonstrates three remarkable emission peaks of the Nd^{3+} cations that correspond to $^4F_{3/2} \rightarrow {}^4I_{9/2}$ (870 and 892 nm), $^4F_{3/2} \rightarrow {}^4I_{11/2}$ (1059 nm), and $^4F_{3/2} \rightarrow {}^4I_{13/2}$ (1334 nm) transitions.[62,63] The excitation spectrogram based on detecting the 1059 nm emission exhibits four striking peaks at 471, 520, 577, and 622 nm (Figure S14a), which can be ascribed to Nd^{3+} $^4I_{9/2} \rightarrow {}^2G_{9/2}/{}^4G_{11/2}/{}^2K_{15/2}$, $^4I_{9/2} \rightarrow {}^4G_{7/2}/{}^4G_{9/2}/{}^2K_{13/2}$, $^4I_{9/2} \rightarrow {}^2G_{7/2}/{}^4G_{5/2}$, and $^4I_{9/2} \rightarrow {}^2H_{11/2}$ transitions, respectively (Table S3).[64] For the purpose of determining the lifetime, the PL lifetime curve of **3** (Figure 7b) based on detecting the strongest emission at 1059 nm abides by the biexponential equation $I = A_1 \exp(-t/\tau_1) + A_2 \exp(-t/\tau_2)$, affording τ_1 and τ_2 of 1.16 μs (28.36%) and 10.70 μs (71.64%), respectively, and the agreement factor (χ^2) of 1.278. According to the average lifetime equation $\tau^* = [A_1\tau_1^2 + A_2\tau_2^2]/[A_1\tau_1 + A_2\tau_2]$, τ^* is calculated to 7.99 μs (Table S4).[65]

The PL emission spectrogram of **4** obtained using the excitation at 402 nm reveals three featured peaks at 563, 599, and 644 nm (Figure 7c) that are attributed to the Sm^{3+} $^4G_{5/2} \rightarrow {}^6H_J$ (J = 5/2, 7/2, 9/2) transitions.[66] The excitation spectrogram of **4** (Figure S14b) based on detecting the 644 nm emission is dominated by the $^6H_{5/2} \rightarrow {}^6P_{3/2}$ transition at 402 nm (Table S3).[66] The PL decay curve of **4** (Figure 7d) on the strongest emission at 644 nm keeps to the biexponential function, engendering τ_1 and τ_2 of 2.50 μs (45.07%) and 9.47 μs (54.93%), respectively, with the agreement factor (χ^2) of 1.013. Thus, τ^* is indexed to 6.33 μs (Table S4).

The emission spectrogram of **5** (Figure 7e) was measured under excitation with a wavelength of 464 nm, which manifests several conspicuous luminescent peaks derived from the Eu^{3+} cations at 526, 537, 556, 585, 592, 615, 651, and 697 nm that can be ascribed to the $^5D_1 \rightarrow {}^7F_J$ (J = 0, 1, 2) and $^5D_0 \rightarrow {}^7F_J$ (J = 0, 1, 2, 3, 4) transitions (Table S3).[66] The magnetic dipole $^5D_0 \rightarrow {}^7F_{1,3}$ transitions are less responsive to the topical microenvironment, whereas the electric dipole $^5D_0 \rightarrow {}^7F_{0,2,4}$ transitions are comparatively hypersensitized to the topical environments.[67] As is known to all, the $^5D_0 \rightarrow {}^7F_0$ emission is sternly forbidden in a symmetrical environment; nonetheless, the $^5D_0 \rightarrow {}^7F_0$ peak at 585 nm appears in **5**, indicating that the Eu^{3+} ion is inhabited in the laigh symmetrical environment. The magnetic dipole $^5D_0 \rightarrow {}^7F_1$ emission intensity at 592 nm hardly changes along with the topical microenvironment of the Eu^{3+} ion, whereas the electric dipole $^5D_0 \rightarrow {}^7F_2$ emission intensity at 615 nm is extremely sensitive to the topical microenvironment. As a rule, the Eu^{3+} ion could be identified as a structure probe to examine its topical microenvironment in a desired compound according to Judd−Ofelt theory.[68,69] When the Eu^{3+} ion is located at a symmetrical microenvironment, the $^5D_0 \rightarrow {}^7F_1$ transition should be dominant, otherwise, the $^5D_0 \rightarrow {}^7F_2$ transition would be preponderant in an asymmetrical microenvironment.[70,71] As demonstrated in Figure 7e, the $^5D_0 \rightarrow {}^7F_{2,4}$ emission intensity is much stronger than the $^5D_0 \rightarrow {}^7F_{1,3}$ emission intensity, indicating that the Eu^{3+} ion does not reside in the inversion symmetrical environment. Moreover, the $^5D_0 \rightarrow {}^7F_2$ emission intensity increases as the topical symmetry of the Eu^{3+} center declines. As a consequence, the $I(^5D_0 \rightarrow {}^7F_2)/I(^5D_0 \rightarrow {}^7F_1)$ emission intensity ratio always serves as a criterion to probe the local circumstance change of the Eu^{3+} ion.[72] In the present paper, the $I(^5D_0 \rightarrow {}^7F_2)/I(^5D_0 \rightarrow {}^7F_1)$ emission intensity ratio for **5** is ca. 3.03, reflecting that the symmetry of the topical microenvironment of the Eu^{3+} ion is low, which coincides with the result of the structure analysis. The excitation spectrogram based on detecting the emission at 617 nm (Figure S14c) indicates four excitation peaks at 384, 394, 416, and 464 nm, which are assigned to $^7F_0 \rightarrow {}^5G_2$, $^7F_0 \rightarrow {}^5L_6$, $^7F_0 \rightarrow {}^5D_3$, and $^7F_0 \rightarrow {}^5D_2$ transitions of the Eu^{3+} ion.[73,74] The PL lifetime curve for **5** was carried out and conforms to a biexponential function, providing τ_1 and τ_2 as 0.58 μs (4.06%) and 18.27 μs (95.94%), respectively, the agreement factor (χ^2) of 1.295, and τ^* of 17.55 μs (Figure 7f, Table S4). However, the average decay times of $K_4Na_4H_4[Eu_2(gly)_4(\alpha\text{-}BW_{11}O_{39})_2]\cdot 23H_2O$ (1.79 ms) in which the Eu^{3+} ions are surrounded by gly and other four oxygens are from the $[\alpha\text{-}BW_{11}O_{39}]^{9-}$ segment but no water ligands encircled[75] and $Na_{0.5}Cs_{4.5}[Eu(\alpha\text{-}SiW_{11}O_{39})\ (H_2O)_2]\cdot 23H_2O$ (0.39 ms) in which the Eu^{3+} ion is coordinated by two water ligands[76] are conspicuously longer than that of **5**, principally stemming from the fluorescence quenching by aqueous ligands.[77] In general, water ligands can lead to PL quenching of the Ln^{3+} ions and further shorten PL decay lifetimes by coupling with proximal OH oscillators,[78] therefore, the shorter lifetime of **5** can be expected. For another, Ln^{3+} cations usually are subjected to feeble luminescence because their absorbance coefficients (<10 $mol^{-1}\cdot L\cdot cm^{-1}$) are very small on account of the spin- and parity-forbidden f−f transitions.[75] It should be noted that organic groups as sensitizing agents can absorb light and delivery energy from organic groups to Ln^{3+} ions through intramolecular energy transfer to overcome this drawback.[63] Taking these two factors into account, the shorter decay time of **5** is probably due to the coordination of water molecules to Eu^{3+} centers impeding the chelation of pic ligands with Eu^{3+} cations, thereby, lessening the nonradiative decay processes.

The emission spectrogram of **7** was collected on excitation at 451 nm and shows two prominent emission bands originating from the $^4F_{9/2}$ level of Dy^{3+} ions appearing at 573 nm ($^6H_{13/2}$) and 662 nm ($^6H_{11/2}$) (Figure 7g).[79] The excitation spectrogram of **7** based on detecting the emission at 575 nm (Figure S14d) comprises five noticeable bands at 352, 366, 388, 427, and 451 nm that are vested in the transitions from $^6H_{15/2}$ to $^6P_{7/2}$, $^6P_{5/2}$, $^4I_{13/2}$, $^4G_{11/2}$, and $^4I_{15/2}$ of the Dy^{3+} ion.[80] The lifetime behavior of **7** obtained on emission at 575 nm (Figure 7h) adheres to a double exponential decay. The fitting parameters are as follows: τ_1 = 1.18 μs (46.18%), τ_2 = 8.81 μs (53.82%), τ^* = 5.59 μs, and χ^2 = 0.950 (Table S4).

The emission spectrogram of **8** measured on excitation at 459 nm demonstrates one appreciable emission peak arising from the $^5F_5$ level of the Ho^{3+} center appearing at 653 nm ($^5I_8$)

DOI: 10.1021/acs.inorgchem.8b02103
Inorg. Chem. 2018, 57, 15079−15092

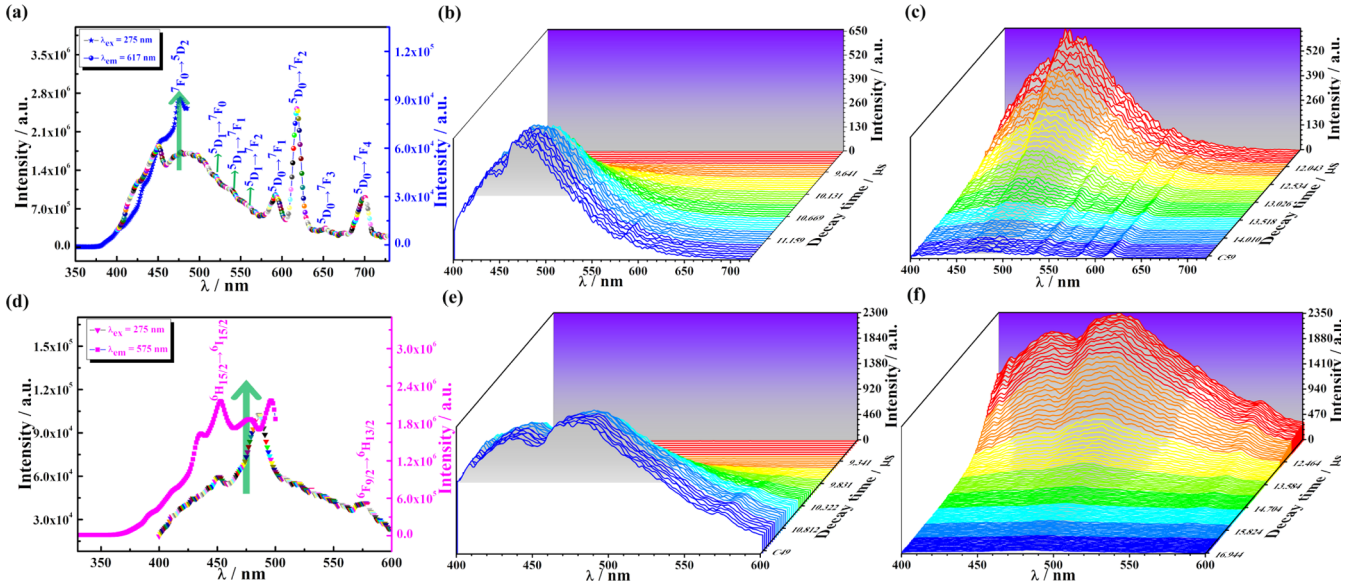

Figure 8. (a) Excitation and emission spectrograms of **5** (λ_{ex} = 275 nm). (b) TRES of **5** (decay time is from 9.2 to 11.6 μs). (c) TRES of **5** (decay time is from 11.6 to 14.6 μs). (d) Excitation and emission spectrograms of **7** (λ_{ex} = 275 nm). (e) TRES of **7** (decay time is from 8.9 to 11.4 μs). (f) TRES of **7** (decay time is from 11.4 to 17.0 μs).

(Figure S15a).[81] The excitation spectrogram of **8** (Figure S15b) displays one band at 459 nm, corresponding to the $^5I_8 \rightarrow {}^4I_{15/2}$ transition of the Ho^{3+} center.[81] The decay time curve of **8** (Figure S15c) obeys a double exponential decay. The fitting parameters are τ_1 = 2.05 μs (52.10%), τ_2 = 10.12 μs (47.90%), χ^2 = 1.037, and τ^* = 5.92 μs (Table S4).

As shown in our above-mentioned crystal structural results, one crystallographically unique Ln^{3+} cation exists in the structures of **4**, **5**, and **7**; as a result, the PL decay behaviors of **4**, **5**, and **7** should conform to a monoexponential function. However, their PL lifetime curves follow a biexponential function, which suggests that there is additional contribution originating from TA fragments in the luminescence procedure. To discover the origin of additional emission contribution, we tested the PL decay curves of $Na_9[B\text{-}\alpha\text{-}SbW_9O_{33}]\cdot 19.5H_2O$. Under the measurement condition of **4**, the PL lifetime decay behavior of $Na_9[B\text{-}\alpha\text{-}SbW_9O_{33}]\cdot 19.5H_2O$ (Figure S16a) acts up to a biexponential equation, leading to τ_1 = 2.07 μs (41.91%), τ_2 = 9.78 μs (58.09%), τ^* = 6.55 μs, and χ^2 = 1.013 (Table S4). Apparently, τ_1 = 2.07 μs and τ_2 = 9.78 μs of $Na_9[B\text{-}\alpha\text{-}SbW_9O_{33}]\cdot 19.5H_2O$ are very approximate to those of **4**, manifesting that the TA fragments play a very crucial part in the PL procedure of **4**, which leads to the biexponential decay behavior of **4**. Under the measurement condition of **5**, the PL lifetime behavior of $Na_9[B\text{-}\alpha\text{-}SbW_9O_{33}]\cdot 19.5H_2O$ was measured and abides by a biexponential decay curve with τ_1 1.86 μs (44.00%) and τ_2 9.99 μs (56.00%) (Figure S16b). The average lifetime was 6.41 μs, and the factor (χ^2) is 0.992 (Table S4). It can be clearly seen that the average lifetime of $Na_9[B\text{-}\alpha\text{-}SbW_9O_{33}]\cdot 19.5H_2O$ is about one-third of the average lifetime of **5**, which strongly demonstrates that the emission procedure of **5** comes from the common contribution of both Eu^{3+} ions and {B-β-SbW_9} fragments. Under the measurement condition of **7**, the PL lifetime behavior of $Na_9[B\text{-}\alpha\text{-}SbW_9O_{33}]\cdot 19.5H_2O$ was measured and adheres to a biexponential equation, accompanying τ_1 1.33 μs (46.61%) and τ_2 8.51 μs (53.39%) (Figure S16c). The average lifetime was 6.41 μs, and the factor (χ^2) is 0.951 (Table S4). Apparently, τ_1 = 1.33 μs and τ_2 = 8.51 μs of $Na_9[B\text{-}\alpha\text{-}SbW_9O_{33}]\cdot 19.5\ H_2O$ is very approximate to those of **7**, indicating that TA fragments also contribute to the luminescence procedure of **7**, which leads to the biexponential decay behavior of **7**. Under the measurement condition of **8**, the PL lifetime behavior of $Na_9[B\text{-}\alpha\text{-}SbW_9O_{33}]\cdot 19.5H_2O$ was measured and follows a biexponential equation with τ_1 1.01 μs (55.98%) and τ_2 9.36 μs (44.02%) (Figure S16d), and the factor (χ^2) of 1.203. The average lifetime is 4.69 μs (Table S4). Overtly, the lifetime values of $Na_9[B\text{-}\alpha\text{-}SbW_9O_{33}]\cdot 19.5H_2O$ are very close to those of **8**, indicating that TA fragments indeed are responsible for the luminescence procedure of **8**, which leads to the biexponential decay behavior of **8**.

Although {SbW_9} fragments and Ln^{3+} ions make joint contributions during the course of the luminescence procedures of **4**, **5**, and **7**, is there energy transfer between {SbW_9} fragments and Ln^{3+} ions or between pic ligands and Ln^{3+} ions? Based on aforementioned structural descriptions, we can clearly see that there are two structure types of **1**−**7**. Therefore, the studies on verifying the energy transfer among the {SbW_9} fragments, pic ligand, and Ln^{3+} ions were described separately. For **1**−**5**, take **5** as an example. At the beginning, the solid-state UV−visible absorption spectra of $Na_9[B\text{-}\alpha\text{-}SbW_9O_{33}]\cdot 19.5H_2O$ and the pic ligand were recorded (Figure S17). The UV−visible absorption spectrum of $Na_9[B\text{-}\alpha\text{-}SbW_9O_{33}]\cdot 19.5H_2O$ clearly shows a broad absorption band at ca. 250−350 nm centered at 275 nm that corresponds to the $O_{b,c} \rightarrow W$ transitions of the {SbW_9} fragments, whereas two absorption peaks at 258 and 295 nm in the UV−visible absorption spectrogram of the pic ligand can be boiled down to the $\pi \rightarrow \pi^*$ or $n \rightarrow \pi^*$ transitions in the pic ligand.[43,82,83] The absorption spectrogram in the UV−visible region of the solid sample of **1** was also recorded to further prove the peak position of {B-β-SbW_9} fragments and pic ligand (Figure S18). Thus, on excitation with a light of 275 nm at ambient temperature, the PL emission spectrum between 400 and 720 nm of **5** was measured to find the emitting bands of {B-β-SbW_9} fragments and pic ligands. The emission spectrum of **5** shows a wide band between 400 and 580 nm and seven characteristic emission peaks of Eu^{3+} ions at 521, 539, 560, 592,

DOI: 10.1021/acs.inorgchem.8b02103
Inorg. Chem. 2018, 57, 15079−15092

617, 652, and 701 nm (Figure 8a, the colorful line). The seven characteristic emission peaks should be attributed to $^5D_1 \rightarrow {}^7F_J$ (J = 0, 1, 2) and $^5D_0 \rightarrow {}^7F_J$ (J = 1, 2, 3, 4) transitions.[68] We conjecture that the broad emission band between 400 and 580 nm in the emission spectrum of **5** may be collectively evoked by the $^3T_{1u} \rightarrow {}^1A_{1g}$ transition stemming from {B-β-SbW_9} fragments and $\pi^* \rightarrow \pi$ or $\pi^* \rightarrow$ n transitions of pic groups. Thus, the emission spectra of the solid-state samples of Na_9[B-α-SbW_9O_{33}]·19.5H_2O and pic were collected on excitation with a light of 275 nm. As demonstrated in Figure S19, the emission spectrogram of Na_9[B-α-SbW_9O_{33}]·19.5H_2O reveals a very broad band between 400 and 650 nm corresponding to the $^3T_{1u} \rightarrow {}^1A_{1g}$ transition of {B-β-SbW_9} fragments,[43,82,83] as illustrated in Figure S20.

The pic ligand also reveals two emission peaks centered at 450 and 484 nm between 400 and 600 nm that are attributable to the $\pi^* \rightarrow \pi$ or $\pi^* \rightarrow$ n transitions.[84,85] Therefore, it can be definitely concluded that the broad emission band in the range of ca. 400−580 nm in the emitting spectrogram of **5** roots in the combined contribution of {B-β-SbW_9} fragments and pic ligands. On the other hand, by monitoring the $^5D_0 \rightarrow {}^7F_2$ emission at 617 nm of Eu^{3+} centers in the emitting spectrogram of **5**, the excitation spectrogram of **5** (Figure 8a, the bule line) was recorded and reveals an excitation peak at 477 nm resulting from the typical $^7F_0 \rightarrow {}^5D_2$ transition of Eu^{3+} centers.[73,74] It can be explicitly observed from Figure 8a that the emission band derived from $^3T_{1u} \rightarrow {}^1A_{1g}$ transition of {B-β-SbW_9} fragment and the $\pi^* \rightarrow \pi$ or $\pi^* \rightarrow$ n transitions of pic components in the emission spectrum of **5** can overlap with the excitation peak ($^7F_0 \rightarrow {}^5D_2$) derived from Eu^{3+} ions in the excitation spectrum of **5**. This phenomenon can testify the energy transfer emergence from {B-β-SbW_9} fragments and pic components to Eu^{3+} centers. To consolidate the energy transfer existence from {B-β-SbW_9} fragments and pic components to Eu^{3+} centers, the time-resolved emission spectrum (TRES) tests of **5** have been performed on excitation with a light of 275 nm in the emission scope of 400−720 nm (Figure 8b,c). During the course of the excitation of **5** (time is from 9.2 to 11.6 μs), clearly, the emission intensities of {B-β-SbW_9} fragments, pic components, and Eu^{3+} centers rapidly increase with prolonging time (Figure 8b). After the emission intensities of **5** reach the strongest, the emission band intensities of {B-β-SbW_9} fragments, components, and Eu^{3+} centers begin to decline as time increases from 11.6 to 14.6 μs (Figure 8c). As time goes on, the PL decay rate of the emission band of {B-β-SbW_9} fragments and pic ligands is much faster than that of the emission peaks of Eu^{3+} centers (Figure 9a), which indicates to some extent the energy transfer from {B-β-SbW_9} fragments and components to Eu^{3+} centers because the sensitization of {B-β-SbW_9} fragments and pic components and Eu^{3+} centers toward the emission of Eu^{3+} centers in some degree alleviates the decrease of the intensity of the emission peaks of Eu^{3+} ions. In addition, the emission color changes in CIE chromaticity diagram (Figure S21) can also demonstrate the existence of energy transfer from {B-β-SbW_9} fragments and pic ligands to Eu^{3+} ions. For **6**−**7**, take **7** as an example. Similar to **5**, based on the UV−visible absorption spectrograms of the solid-state samples of Na_9[B-α-SbW_9O_{33}]·19.5H_2O and the pic ligand and **6** (Figures S17 and S22), we still use the excitation at 275 nm to collect the PL emission spectrogram of **7**. The PL emission spectrogram of **7** in 400−600 nm is displayed in Figure 8d in a colorful line. Similarly, the broad emission peak at 400−580 nm is assigned to {B-β-SbW_9} fragments and pic components,[43,82,83] and the weak emission peak at 575 nm is

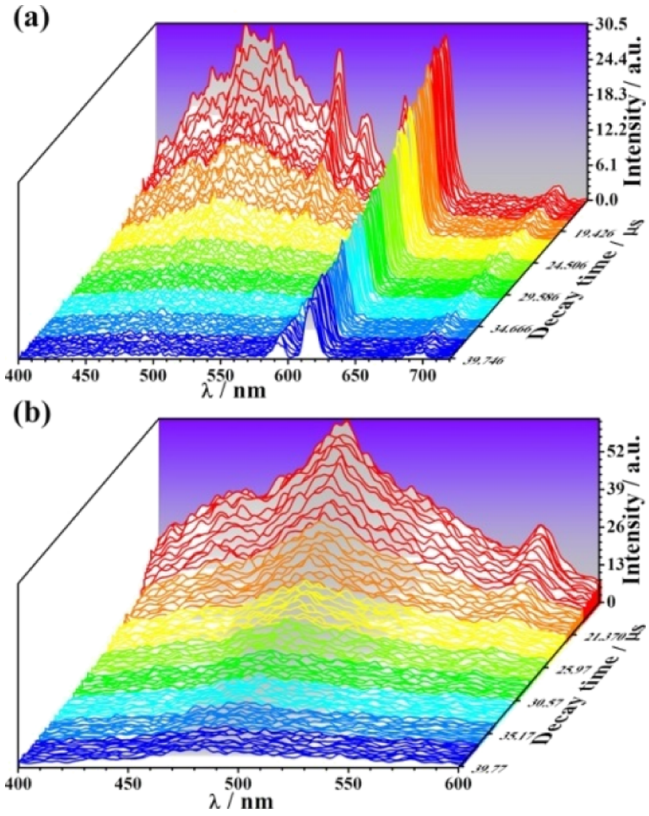

Figure 9. (a) TRES of **5** from 14.6 to 40.0 μs. (b) TRES of **7** from 17.0 to 40.0 μs.

attributable to the Dy^{3+} $^4F_{9/2} \rightarrow {}^6H_{13/2}$ transition.[79] By monitoring the emission peak at 575 nm of **7**, the excitation spectrogram of **7** (Figure 8d, the purple line) was obtained and exhibits an obvious excitation peak at 451 nm assigned to the Dy^{3+} $^6H_{15/2} \rightarrow {}^4I_{15/2}$ transition.[80] Notably, the emission band derived from $^3T_{1u} \rightarrow {}^1A_{1g}$ transition of {B-β-SbW_9} fragment and the $\pi^* \rightarrow \pi$ or $\pi^* \rightarrow$ n transitions of pic components in the emission spectrogram of **7** can be superimposed on the excitation band derived from Dy^{3+} $^6H_{15/2} \rightarrow {}^4I_{15/2}$ transition in the excitation spectrogram of **7**, which proves the presence of energy transfer from {B-β-SbW_9} fragment and pic ligands to Dy^{3+} ions (Figure 8d).[80] Furthermore, the TRES measurements of **7** were also performed on excitation with a light of 275 nm in the emission scope of 400−600 nm (Figure 8e,f). In the photoexcitation procedure of **7** (time is from 8.9 to 11.4 μs), apparently, the emission intensities of {B-β-SbW_9} fragments, pic components, and Dy^{3+} ions quickly enhance with increasing time (Figure 8e). When the emission intensities reach the strongest, the emission intensities of {B-β-SbW_9} fragments, pic components, and Dy^{3+} ions begin to decline over the time increase from 11.4 to 17.0 μs (Figure 8f). With time elapsing, the PL decay rate of the emission bands of {B-β-SbW_9} fragments and pic components is faster than that of the emission peaks of Dy^{3+} ions (Figure 9b), which manifests to a certain degree the existence of energy transfer from {B-β-SbW_9} fragments and pic components to Dy^{3+} ions because the sensitization of {B-β-SbW_9} fragments and pic components toward the emission of Dy^{3+} ions in some degree inhibits the decrease of the intensity of the emission peaks of Dy^{3+} ions. Moreover, the emission color changes in CIE chromaticity diagram (Figure S23) can also demonstrate that the existence of energy transfer from {B-β-SbW_9} fragments and pic components to Dy^{3+} ions. In a word,

DOI: 10.1021/acs.inorgchem.8b02103
Inorg. Chem. 2018, 57, 15079−15092

the energy transfer from {B-β-SbW_9} fragments and pic components to Ln^{3+} ions occurs in the emission processes of **5** and **7**.

The CIE 1931 chromatic diagram provides the commodious approach to probe the probable colors through the comprehensive utilization of three basic colors, which is generally used to tune the emission color variation and the emission intensity change, hence, the control of the color trueness has been utilized to the fields in lighting and display devices.[86] In the chromatic diagram, the chromaticity coordinates (x, y) are used to confirm the accurate emitting color of a given sample when the white light emission is defined at the center position (x = 0.33333, y = 0.33333). Herein, x is the red-to-blue ratio, whereas y is the green-to-blue ratio. The (x, y) of **4** (0.48969, 0.48014), **5** (0.54043, 0.44766), **7** (0.38993, 0.54866), and **8** (0.60343, 0.39260) converted from their corresponding emission spectra are revealed in Figure 10. Furthermore, the CIE chromaticity

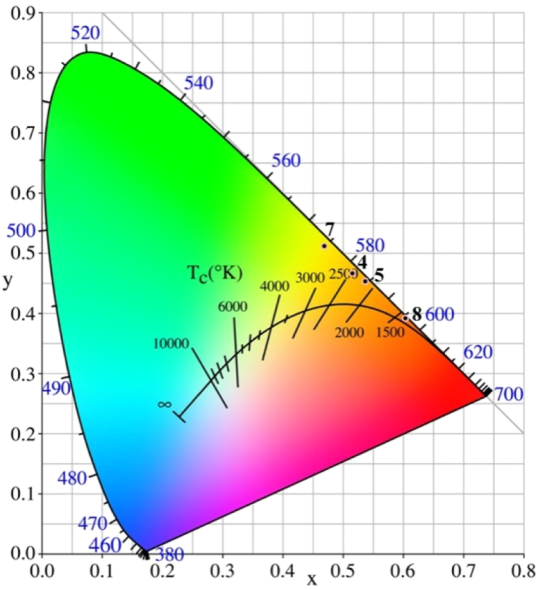

Figure 10. Exhibition of the emission colors of **4**, **5**, **7**, and **8** in the CIE chromatic diagram.

space can also show the CT (T_c). The CT of a light source is the temperature of an ideal black-body radiator that radiates light of a color comparable to that of the light source, which has been used in some vital fields such as photography, horticulture, videography, and so forth[87,88] Herein, CTs of **4**, **5**, **7**, and **8** are 2731, 2020, 4557, and 1685 K, respectively.

CONCLUSIONS

In summary, we report three types of pic-decorated DFH Keggin-type TAs **1**−**9**, which represent the first DFH TAs functionalized by monocarboxylic aromatic ligands. The 3-D heterometallic frameworks of **1**−**5** are constructed from quadripic-inserted Krebs-type $[Fe_4(H_2O)_2(pic)_4(B\text{-}\beta\text{-}SbW_9O_{33})_2]^{10-}$ subunits linked via hydrated $[Ln(H_2O)_5]^{3+}$ cations and pic ligands, whereas the molecular units of **6**−**7** consist of two kinds of quadripic-inserted non-Krebs-type $[Fe_2W_4O_9(H_2O)_2(Hpic)_4(B\text{-}\beta\text{-}SbW_9O_{33})_2]^{6-}$ and $\{[Ln(H_2O)_8]_2[Fe_4W_2O_7(H_2O)_4(pic)_2(Hpic)_2(B\text{-}\beta\text{-}SbW_9O_{33})_2]\}^{4-}$ subunits. The 1-D DFH double chain of **8**−**9** is assembled from two crystallographically independent $\{[Ln(H_2O)_6]_2[Fe_4(H_2O)_2(Hpic)_2(pic)_2(B\text{-}\beta\text{-}SbW_9O_{33})_2]\}^{2-}$ subunits through Ln^{3+} linkers. The PL spectra and lifetime behaviors of **3**, **4**, **5**, **7**, and **8** have been carried out. Moreover, further PL studies of **4**, **5**, **7**, and **8** demonstrate that the {B-β-SbW_9} fragments, pic components, and Ln^{3+} ions make the joint contributions during the course of the luminescence procedures. In addition, **5** and **7** were chosen as representatives to explore the energy transfer among the {B-β-SbW_9} fragments, pic components, and Ln^{3+} ions and the results indicate that energy transfer from {B-β-SbW_9} fragments and pic components to Ln^{3+} ions occurs in the emission processes of **5** and **7**. In a word, this work presents a great rational synthetic strategy of constructing organic−inorganic DFH TA hybrids. To construct novel DFH POMOIHMs, our following work will have these three aspects: (i) other trilacunary precursors containing the effects of the lone-electrons pair can be employed; (ii) aromatic polycarboxylic acid ligands could be imported to our reaction; and (iii) considering the combination function of flexible ligands and rigid ligands, two or more types of carboxylate ligands can be introduced to our research system.

ASSOCIATED CONTENT

Supporting Information

The Supporting Information is available free of charge on the ACS Publications website at DOI: 10.1021/acs.inorgchem.8b02103.

BVS results, Ln−O distances, pertinent structure diagrams, PXRD figures, TG figures, IR spectra, pertinent PL spectra, solid-state UV-visible absorption spectra, solid-state emission spectra, emission color changes in CIE chromaticity diagrams, lifetime decay curves, crystallographic data and structure refinements, and excitation/emission peaks (PDF)

Accession Codes

CCDC 1820582−1820588 for **1**−**7** and 1868327−1868328 for **8**−**9** contain the supplementary crystallographic data for this paper. These data can be obtained free of charge via www.ccdc.cam.ac. uk/data_request/cif, or by emailing data_request@ccdc.cam.ac.uk, or by contacting The Cambridge Crystallographic Data Centre, 12, Union Road, Cambridge CB2 1EZ, UK; Fax: +44 1223 336033.

AUTHOR INFORMATION

Corresponding Authors

*E-mail: ljchen@henu.edu.cn (L.C).
*E-mail: zhaojunwei@henu.edu.cn (J.Z.).

ORCID

Junwei Zhao: 0000-0002-7685-1309

Notes

The authors declare no competing financial interest.

ACKNOWLEDGMENTS

We thank the National Natural Science Foundation of China (21771052, 21671054, 21571048, 21871077), the Innovation Scientists and Technicians Troop Construction Projects of Henan Province (174100510016), the Program for Science & Technology Innovation Talents in Universities of Henan Province (16HASTIT001), and the 2014 Special Foundation for Scientific Research Project of Henan University (XXJC20140001).

DOI: 10.1021/acs.inorgchem.8b02103
Inorg. Chem. 2018, 57, 15079−15092

REFERENCES

(1) Sharma, R. K.; Sharma, S.; Dutta, S.; Zboril, R.; Gawande, M. B. Silica-nanosphere-based organic−inorganic hybrid nanomaterials: synthesis, functionalization and applications in catalysis. *Green Chem.* **2015**, *17*, 3207−3230.

(2) Song, Y.-F.; Cronin, L. Postsynthetic Covalent modification of metal− organic framework (MOF) materials. *Angew. Chem., Int. Ed.* **2008**, *47*, 4635−4637.

(3) Dang, D.; Wu, P.; He, C.; Xie, Z.; Duan, C. Homochiral metal−organic frameworks for heterogeneous asymmetric catalysis. *J. Am. Chem. Soc.* **2010**, *132*, 14321−14323.

(4) Ikeda, T.; Hiyoshi, N.; Matsuura, S.-i.; Kodaira, T.; Nakaoka, T.; Irisa, A.; Kawano, M.; Yamamoto, K. Amphiphilic organic−inorganic hybrid zeotype aluminosilicate like a nanoporous crystallized Langmuir−Blodgett film. *Angew. Chem., Int. Ed.* **2015**, *54*, 7994−7998.

(5) Hu, J.-F.; Han, T.; Chi, Y.-N.; Lin, Z.-G.; Xu, Y.-Q.; Yang, S.; Wei, D.; Zheng, Y.-Z.; Hu, C.-W. Sulfur-centred polyoxoniobate-based 3D organic−inorganic hybrid compound and its magnetic behavior. *Chem. Commun.* **2016**, *52*, 10846−10849.

(6) Wu, J.; Akhtar, N.; Gengler, R. Y. N.; Palstra, T. T. M.; Rudolf, P. Generating new magnetic properties in organic−inorganic hybrids. *J. Mater. Chem. C* **2017**, *5*, 1782−1788.

(7) Cheng, C.-C.; Chu, Y.-L.; Chu, C.-W.; Lee, D.-J. Highly efficient organic−inorganic electroluminescence materials for solution-processed blue oganic light-emitting diodes. *J. Mater. Chem. C* **2016**, *4*, 6461−6465.

(8) Yao, Q.; Fang, H.; Deng, K.; Kan, E.; Jena, P. Superhalogens as building blocks of two-dimensional organic−inorganic hybrid perovskites for optoelectronics applications. *Nanoscale* **2016**, *8*, 17836−17842.

(9) Liu, J.; Luo, J.; Han, Q.; Cao, J.; Chen, L.; Song, Y.; Zhao, J. Coexistence of long-range ferromagnetic orderingand spin-glass behavior observed in the firstinorganic−organic hybrid 1-D oxalate-bridgingnona-Mn^{II} sandwiched tungstoantimonate chain. *J. Mater. Chem.* **2017**, *5*, 2043−2055.

(10) Li, H.-L.; Liu, Y.-J.; Liu, J.-L.; Chen, L.-J.; Zhao, J.-W.; Yang, G.-Y. Structural transformation from dimerization to tetramerization of serine-decorated rare-earth-incorporated arsenotungstates induced by the usage of rare-earth salts. *Chem.—Eur. J.* **2017**, *23*, 2673−2689.

(11) Yin, Q.; Tan, J. M.; Besson, C.; Geletii, Y. V.; Musaev, D. G.; Kuznetsov, A. E.; Luo, Z.; Hardcastle, K. I.; Hill, C. L. A fast soluble carbon-free molecular water oxidation catalyst based on abundant metals. *Science* **2010**, *328*, 342−345.

(12) Clemente-Juan, J. M.; Coronado, E.; Gaita-Ariño, A. Magnetic polyoxometalates: from molecular magnetism to molecular spintronics and quantum computing. *Chem. Soc. Rev.* **2012**, *41*, 7464−7478.

(13) Long, D.-L.; Tsunashima, R.; Cronin, L. Polyoxometalates: building blocks for functional nanoscale systems. *Angew. Chem., Int. Ed.* **2010**, *49*, 1736−1758.

(14) Berzelius, J. J. The Preparation of Phosphomolybdate Ion $[PMo_{12}O_{40}]^{3-}$. *Ann. Phys.* **1826**, *82*, 369−392.

(15) Hill, C. L. Introduction: polyoxometalates multicomponent molecular vehicles to probe fundamental issues and practical problems. *Chem. Rev.* **1998**, *98*, 1−2.

(16) Zhao, J.-W.; Li, Y.-Z.; Chen, L.-J.; Yang, G.-Y. Research progress on polyoxometalate-based transition-metal−rare-earth heterometallic derived materials: synthetic strategies, structural overview and functional applications. *Chem. Commun.* **2016**, *52*, 4418−4445.

(17) Jiang, C.; Lesbani, A.; Kawamoto, R.; Uchida, S.; Mizuno, N. Channel-selective independent sorption and collection of hydrophilic and hydrophobic molecules by $Cs_2[Cr_3O(OOCC_2H_5)_6(H_2O)_3]_2[\alpha$-$SiW_{12}O_{40}]$ ionic crystal. *J. Am. Chem. Soc.* **2006**, *128*, 14240−14241.

(18) Liu, J.-C.; Han, Q.; Chen, L.-J.; Zhao, J.-W.; Streb, C.; Song, Y.-F. Aggregation of giant cerium−bismuth tungstate clusters into a 3D porous framework with gigh proton conductivity. *Angew. Chem., Int. Ed.* **2018**, *57*, 8416−8420.

(19) Kortz, U.; Müller, A.; van Slageren, J.; Schnack, J.; Dalal, N. S.; Dressel, M. Polyoxometalates: fascinating structures, unique magnetic properties. *Coord. Chem. Rev.* **2009**, *253*, 2315−2327.

(20) Zheng, S.-T.; Yang, G.-Y. Recent advances in paramagnetic-TM-substituted polyoxometalates. *Chem. Soc. Rev.* **2012**, *41*, 7623−7646.

(21) Wang, Y.; Weinstock, I. A. Polyoxometalate-decorated nanoparticles. *Chem. Soc. Rev.* **2012**, *41*, 7479−7496.

(22) Zhao, J.-W.; Li, Y.-Z.; Chen, L.-J.; Yang, G.-Y. Research progress on polyoxometalate-based transition-metal−rare-earth heterometallic derived materials: synthetic strategie. *Chem. Commun.* **2016**, *52*, 4418−4445.

(23) Liu, H.; Qin, C.; Wei, Y.-G.; Xu, L.; Gao, G.-G.; Li, F.-Y.; Qu, X.-S. Copper-complex-linked polytungsto-bismuthate (-antimonite) chain containing sandwich Cu(II) ions partially modified with imidazole ligand. *Inorg. Chem.* **2008**, *47*, 4166−4172.

(24) Tian, S.; Li, Y.; Zhao, J.; Ma, P.; Chen, L. A novel organic−inorganic hybrid sandwich-type germanotungstate with discrete $[Fe_4(en)_2(\alpha$-$GeW_9O_{34})_2]^{8-}$ polyoxoanions and 1-D $[Fe_4(en)(\alpha$-$GeW_9O_{34})_2]_n^{8n-}$ polymeric chains. *Inorg. Chem. Commun.* **2013**, *33*, 99−104.

(25) Sang, X.; Li, J.; Zhang, L.; Wang, Z.; Chen, W.; Zhu, Z.; Su, Z.; Wang, E. A novel carboxyethyltin functionalized sandwich-type germanotungstate: synthesis, crystal structure, photosensitivity, and application in dye-sensitized solar cells. *ACS Appl. Mater. Interfaces* **2014**, *6*, 7876−7884.

(26) Hussain, F.; Sandriesser, S.; Speldrich, M.; Patzke, G. R. A new series of lanthanoid containing Keggin-type germanotungstates with acetate chelators: $[\{Ln(CH_3COO)GeW_{11}O_{39}(H_2O)\}_2]^{12-}${Ln=$Eu^{III}$, Gd^{III}, Tb^{III}, Dy^{III}, Ho^{III}, Er^{III}, Tm^{III}, and Yb^{III}}. *J. Solid State Chem.* **2011**, *184*, 214−219.

(27) Feng, X.-J.; Han, H.-Y.; Wang, Y.-H.; Li, L.-L.; Li, Y.-G.; Wang, E.-B. Assembly of chainlike polyoxometalate-based lanthanide complexes in one-pot reaction system. *CrystEngComm* **2013**, *15*, 7267−7273.

(28) Li, S.; Wang, Y.; Ma, P.; Wang, J.; Niu, J. From a versatile arsenotungstate precursor to a large lanthanide-containing polyoxometalate −carboxylate hybrid. *CrystEngComm* **2014**, *16*, 10746−10749.

(29) Ju, W.-W.; Zhang, H.-T.; Xu, X.; Zhang, Y.; Xu, Y. Enantiomerically pure lanthanide−organic polytungstates exhibiting two-photon absorption properties. *Inorg. Chem.* **2014**, *53*, 3269−3271.

(30) Li, L.-L.; Han, H.-Y.; Wang, Y.-H.; Tan, H.-Q.; Zang, H.-Y.; Li, Y.-G. Construction of polyoxometalates from dynamic lacunary polyoxotungstate building blocks and lanthanide linkers. *Dalton Trans.* **2015**, *44*, 11429−11436.

(31) Reinoso, S.; Galán-Mascarós, J. R.; Lezama, L. A new type of heterometallic 3d−4f rhomblike core in Weakley-like polyoxometalates. *Inorg. Chem.* **2011**, *50*, 9587−9593.

(32) Shi, D.-Y.; Zhao, J.-W.; Chen, L.-J.; Ma, P.-T.; Wang, J.-P.; Niu, J.-Y. Four Types of 1D or 2D organic−inorganic hybrids assembled by arsenotungstates and Cu^{II}−$Ln^{III/IV}$heterometals. *CrystEngComm* **2012**, *14*, 3108−3119.

(33) Zhao, H.-Y.; Zhao, J.-W.; Yang, B.-F.; He, H.; Yang, G.-Y. Novel three- dimensional organic−inorganic heterometallic hybrid built by sandwich-type tetra-Mn-substituted germanotungstates through mixed 3d and 4f metal linkers. *Cryst. Growth Des.* **2013**, *13*, 5169−5174.

(34) Yao, S.; Yan, J.-H.; Duan, H.; Jia, Q.-Q.; Zhang, Z.-M.; Wang, E.-B. Heterometallic 3d−4f cluster-containing polyoxotungstate obtained by partial disassembly of preformed large clusters. *RSC Adv.* **2015**, *5*, 76206−76210.

(35) Chen, L.; Cao, J.; Li, X.; Ma, X.; Luo, J.; Zhao, J. The first purely inorganic polyoxotungstates constructed from dimeric tungstoantimonate -based iron−rare-earth heterometallic fragments. *CrystEngComm* **2015**, *17*, 5002−5013.

(36) Artetxe, B.; Reinoso, S.; Felices, L. S.; Lezama, L.; Gutiérrez-Zorrilla, J. M.; Vicent, C.; Haso, F.; Liu, T. New perspectives for old clusters: Anderson−Evans anions as building blocks of large polyoxometalate frameworks in a series of heterometallic 3d−4 f species. *Chem.—Eur. J.* **2016**, *22*, 4616−4625.

(37) Zhao, J.-W.; Cao, J.; Li, Y.-Z.; Zhang, J.; Chen, L.-J. First tungstoantimonate-based transition-metal−lanthanide heterometallic

DOI: 10.1021/acs.inorgchem.8b02103
Inorg. Chem. 2018, 57, 15079−15092

hybrids functionalized by amino acid ligands. *Cryst. Growth Des.* **2014**, *14*, 6217−6229.
(38) Chen, L.; Zhang, F.; Ma, X.; Luo, J.; Zhao, J. Two types of novel tetra-iron substituted sandwich-type arsenotungastates with supporting lanthanide pendants. *Dalton Trans.* **2015**, *44*, 12598−12612.
(39) Zhao, J.-W.; Li, Y.-Z.; Ji, F.; Yuan, J.; Chen, L.-J.; Yang, G.-Y. Syntheses, structures and electrochemical properties of a class of 1-D double chain polyoxotungstate hybrids $[H_2dap][Cu(dap)_2]_{0.5}[Cu(dap)_2(H_2O)][Ln(H_2O)_3(\alpha\text{-}GeW_{11}O_{39})]\cdot 3H_2O$. *Dalton Trans.* **2014**, *43*, 5694−5706.
(40) Bösing, M.; Loose, I.; Pohlmann, H.; Krebs, B. New strategies for the generation of large heteropolymetalate clusters: the β-B-SbW_9fragment as a multifunctional unit. *Chem.—Eur. J.* **1997**, *3*, 1232−1237.
(41) Loose, I.; Droste, E.; Bösing, M.; Pohlmann, H.; Dickman, M. H.; Rosu, C.; Pope, M. T.; Krebs, B. Heteropolymetalate clusters of the subvalent main group elements Bi^{III} and Sb^{III}. *Inorg. Chem.* **1999**, *38*, 2688−2694.
(42) Dolbecq, A.; Compain, J.-D.; Mialane, P.; Marrot, J.; Rivière, E.; Sécheresse, F. Water substitution on iron centers: from 0D to 1D sandwich typepolyoxotungstates. *Inorg. Chem.* **2008**, *47*, 3371−3378.
(43) Yamase, T. Photo- and electrochromism of polyoxometalates and related materials. *Chem. Rev.* **1998**, *98*, 307−326.
(44) Binnemans, K. Lanthanide-based luminescent hybrid materials. *Chem. Rev.* **2009**, *109*, 4283−4374.
(45) *SAINT* V 6.01 (NT) Software for the CCD Detector System; Bruker Analytical X-ray Systems: Madison, WI, 1999.
(46) Zhang, S.; Zhao, J.; Ma, P.; Niu, J.; Wang, J. Rare-earth−transition-metal organic−inorganic hybrids based on Keggin-type polyoxometalates and pyrazine-2,3-dicarboxylate. *Chem.−Asian J.* **2012**, *7*, 966−974.
(47) Niu, J.; Zhang, S.; Chen, H.; Zhao, J.; Ma, P.; Wang, J. 1-D, 2-D and 3-D organic−inorganic hybrids assembled from Keggin-type polyoxometalates and 3d-4f heterometals. *Cryst. Growth Des.* **2011**, *11*, 3769−3777.
(48) Zhao, J.-W.; Jia, H.-P.; Zhang, J.; Zheng, S.-T.; Yang, G.-Y. A combination of lacunary polyoxometalates and high-nuclear transition-metal clusters under hydrothermal conditions. partII: from double cluster, dimer, and tetramer to three-dimensional frameworks. *Chem.—Eur. J.* **2007**, *13*, 10030−10045.
(49) Rabenau, A. The role of hydrothermal synthesis in preparative chemistry. *Angew. Chem., Int. Ed.* **1985**, *24*, 1026−1040.
(50) Hagrman, P. J.; Hagrman, D.; Zubieta, J. Organic−inorganic hybrid materials: from "simple" coordination polymers to organodiamine-templated molybdenum oxides. *Angew. Chem., Int. Ed.* **1999**, *38*, 2638−2684.
(51) Zhang, S.; Wang, K.; Zhang, D.; Ma, P.; Niu, J.; Wang, J. 2-D and 3-D organic−inorganic hybrid lanthanide molybdates linking by pyridine-2,5-dicarboxylate. *CrystEngComm* **2012**, *14*, 8677−8683.
(52) Zhang, Z.-M.; Li, Y.-G.; Yao, S.; Wang, E.-B. Hexameric polyoxometalates decorated by six 3d−4f heterometallic clusters. *Dalton Trans.* **2011**, *40*, 6475−6479.
(53) Ritchie, C.; Miller, C. E.; Boskovic, C. The generation of a novel polyoxometalate-based 3D framework following picolinate-chelation of tungsten and potassium centres. *Dalton Trans.* **2011**, *40*, 12037−12309.
(54) Ritchie, C.; Baslon, V.; Moore, E. G.; Reber, C.; Boskovic, C. Sensitization of lanthanoid luminescence by organic and inorganic ligands in lanthanoid-organic-polyoxometalates. *Inorg. Chem.* **2012**, *51*, 1142−1151.
(55) McGlone, T.; Vilà-Nadal, L.; Miras, H. N.; Long, D.-L.; Poblet, J. M.; Cronin, L. Assembly of titanium embedded polyoxometalates with unprecedented structural features. *Dalton Trans.* **2010**, *39*, 11599−11604.
(56) Ismail, A. H.; Bassil, B. S.; Römer, I.; Kortz, U. Mono- and di-lanthanide derivatives of 22-tungsto-2-antimonate(III), $[Ln(H_2O)_4Sb_2W_{21}O_{72}(OH)]^{10-}$ and $[Ln_2(H_2O)_8Sb_2W_{20}O_{70})]^{8-}$. *Z. Anorg. Allg. Chem.* **2013**, *639*, 2510−2515.
(57) Kortz, U.; Savelieff, M. G.; Bassil, B. S.; Keita, B.; Nadjo, L. Synthesis and characterization of iron(III)-substituted, dimeric polyoxotungstates, $[Fe_4(H_2O)_{10}(\beta\text{-}XW_9O_{33})_2]^{n-}$ (n = 6, X = As^{III}, Sb^{III}; n = 4, X = Se^{IV}, Te^{IV}). *Inorg. Chem.* **2002**, *41*, 783−789.
(58) Carr, R.; Evans, N. H.; Parker, D. Lanthanide complexes as chiral probes exploiting circularly polarized luminescence. *Chem. Soc. Rev.* **2012**, *41*, 7673−7686.
(59) Heine, J.; Müller-Buschbaum, K. Engineering metal-based luminescence in coordination polymers and metal−organic frameworks. *Chem. Soc. Rev.* **2013**, *42*, 9232−9242.
(60) Isaac, M.; Denisov, S. A.; Roux, A.; Imbert, D.; Jonusauskas, G.; McClenaghan, N. D.; Sénèque, O. Lanthanide luminescence modulation by cation−p interaction ina bioinspired scaffold: selective detection of copper(I). *Angew. Chem.* **2015**, *127*, 11615−11618.
(61) Bünzli, J.-C. G.; Piguet, C. Taking advantage of luminescent lanthanide ions. *Chem. Soc. Rev.* **2005**, *34*, 1048−1077.
(62) Lian, X.; Zhao, D.; Cui, Y.; Yang, Y.; Qian, G. A near infrared luminescent metal−organic framework for temperature sensing in the physiological range. *Chem. Commun.* **2015**, *51*, 17676−17679.
(63) Zhao, D.; Zhang, J.; Yue, D.; Lian, X.; Cui, Y.; Yang, Y.; Qian, G. A highly sensitive near-infrared luminescent metal−organic framework thermometer in the physiological range. *Chem. Commun.* **2016**, *52*, 8259−8262.
(64) Chorazy, S.; Nakabayashi, K.; Arczynski, M.; Pełka, R.; Ohkoshi, S.-i.; Sieklucka, B. Multifunctionality in bimetallic $Ln^{III}[W^{V}(CN)_8]^{3-}$ (Ln=Gd, Nd) coordination helices: optical activity, luminescence, and magnetic coupling. *Chem.—Eur. J.* **2014**, *20*, 7144−7159.
(65) Fujii, T.; Kodaira, K.; Kawauchi, O.; Tanaka, N.; Yamashita, H.; Anpo, M. Photochromic behavior in the fluorescence spectra of 9-anthrol encapsulated in Si−Al glasses prepared by the sol−gel method. *J. Phys. Chem. B* **1997**, *101*, 10631−10637.
(66) Meza-Rocha, A. N.; Speghini, A.; Bettinelli, M.; Caldiño, U. Orange and reddish-orange light emitting phosphors: Sm^{3+} and Sm^{3+}/Eu^{3+} doped zinc phosphate glasses. *J. Lumin.* **2015**, *167*, 305−309.
(67) Álvarez, E.; Zayas, M. E.; Alvarado-Rivera, J.; Félix-Domínguez, F.; Duarte-Zamorano, R. P.; Caldiño, U. New reddish-orange and greenish-yellow light emitting phosphors: Eu3+ and Tb^{3+}/Eu^{3+} in sodium germanate glass. *J. Lumin.* **2014**, *153*, 198−202.
(68) Judd, B. R. Optical absorption intensities of rare-earth ions. *Phys. Rev.* **1962**, *127*, 750−761.
(69) Jost, R.; Lombardi, M.; Derouard, J.; Freund, F. S.; Miller, T. A.; Zegarski, B. R. Singlet−triplet anticrossings and the electronic isotope shift in D_2. *Chem. Phys. Lett.* **1976**, *37*, 507−511.
(70) Kirby, A. F.; Richardson, F. S. Detailed analysis of the optical absorption and emission spectra of europium (3+) in the trigonal (C3) $Eu(DBM)_3\bullet H_2O$ system. *J. Phys. Chem.* **1983**, *87*, 2544−2556.
(71) Stouwdam, J. W.; van Veggel, F. C. J. M. Near-infrared emission of redispersible Er^{3+}, Nd^{3+}, and Ho^{3+}doped LaF_3nanoparticles. *Nano Lett.* **2002**, *2*, 733−737.
(72) Zhang, T.; Spitz, C.; Antonietti, M.; Faul, C. F. J. Highly photoluminescent polyoxometaloeuropate-surfactant complexes by ionic self-assembly. *Chem.—Eur. J.* **2005**, *11*, 1001−1009.
(73) Shi, F.; Meng, J.; Ren, Y.; Su, Q. Structure and luminescence properties of some new $AgLnW_2O_8$compounds. *J. Mater. Chem.* **1997**, *7*, 773−776.
(74) Shen, X.; Yan, B. A novel fluorescence probe for sensing organic amine vapors from a $Eu^{3+}\beta$-Diketonate functionalized bio-MOF-1 hybrid system. *J. Mater. Chem. C* **2015**, *3*, 7038−7044.
(75) Liu, J.; Yu, J.; Han, Q.; Wen, Y.; Chen, L.; Zhao, J. First quadruple-glycine bridging mono-lanthanide-substituted borotungstate hybrids. *Dalton Trans.* **2016**, *45*, 16471−16484.
(76) Mialane, P.; Lisnard, L.; Mallard, A.; Marrot, J.; Antic-Fidancev, E.; Aschehoug, P.; Vivien, D.; Sécheresse, F. Solid-State and Solution Studies of $\{Lnn(SiW_{11}O_{39})\}$ Polyoxoanions: An Example of Building Block Condensation Dependent on the Nature of the Rare Earth. *Inorg. Chem.* **2003**, *42*, 2102−2108.
(77) Beeby, A.; Clarkson, I. M.; Dickins, R. S.; Faulkner, S.; Parker, D.; Royle, L.; de Sousa, A. S.; Williams, J. A. G.; Woods, M. Non-radiative deactivation of the excited states of europium, terbium and ytterbium complexes by proximate energy-matched OH, NH and CH oscillators:

DOI: 10.1021/acs.inorgchem.8b02103
Inorg. Chem. 2018, 57, 15079−15092

an improved luminescence method for establishing solution hydration states. *J. Chem. Soc., Perkin Trans. 2* **1999**, 493−504.
(78) Ritchie, C.; Moore, E. G.; Speldrich, M.; Kögerler, P.; Boskovic, C. Terbium polyoxometalate organic complexes:correlation of structure with luminescence properties. *Angew. Chem., Int. Ed.* **2010**, *49*, 7702−7705.
(79) Singh, N. S.; Sahu, N. K.; Bahadur, D. Multicolor tuning and white light emission from lanthanide doped $YPVO_4$ nanorods: energy transfer studies. *J. Mater. Chem. C* **2014**, *2*, 548−555.
(80) Liu, Y.; Liu, G.; Wang, J.; Dong, X.; Yu, W. Single- component and warm-white-emitting phosphor $NaGd(WO_4)_2$:Tm^{3+}, Dy^{3+}, Eu^{3+}: synthesis, luminescence, energy transfer, and tunable color. *Inorg. Chem.* **2014**, *53*, 11457−11466.
(81) Guan, M.; Zheng, H.; Huang, Z.; Ma, B.; Molokeev, M. S.; Huang, S.; Mei, L. Ca/Sr ratio dependent structure and up-conversion luminescence of $(Ca_{1-x}Sr_x)In_2O_4Yb^{3+}/Ho^{3+}$ phosphors. *RSC Adv.* **2015**, *5*, 59403−59407.
(82) Yamase, T.; Sugeta, M. Charge-transfer photoluminescence of polyoxo-tungstates and -molybdates. *J. Chem. Soc., Dalton Trans.* **1993**, 759−765.
(83) Sengar, M.; Narula, A. K. Luminescent lanthanide complexes based on pyridine-2,6-dicarboxamide and 1,2,4-triazole-3-carboxylic acid ligands as F^- anion sensor. *Sens. Actuators, B* **2017**, *241*, 567−576.
(84) Zhang, L.-P.; Ma, J.-F.; Yang, J.; Pang, Y.-Y.; Ma, J.-C. Series of 2D and 3D coordination polymers based on 1,2,3,4-benzenetetracarboxylate and N-donor ligands: synthesis, topological structures, and photoluminescent properties. *Inorg. Chem.* **2010**, *49*, 1535−1550.
(85) Wang, X.; Qin, C.; Wang, E.; Li, Y.; Hao, N.; Hu, C.; Xu, L. Syntheses, structures, and photoluminescence of a novel class of d^{10} metal complexes constructed from pyridine-3,4-dicarboxylic acid with different coordination architectures. *Inorg. Chem.* **2004**, *43*, 1850−1856.
(86) Zhang, Y.; Gong, W.; Yu, J.; Pang, H.; Song, Q.; Ning, G. A New single-phase white-light-emitting $CaWO_4$:Dy^{3+} phosphor: synthesis, luminescence and energy transfer. *RSC Adv.* **2015**, *5*, 62527−62533.
(87) Wang, Q.; Xu, H.; Zhang, F.; Wang, Z. Influence of color temperature on comfort and preference for LED indoor lighting. *Optik* **2017**, *129*, 21−29.
(88) Kapogiannatou, A.; Paronis, E.; Paschidis, K.; Polissidis, A.; Kostomitsopoulos, N. G. Effect of light colour temperature and intensity on the behaviour of male C57CL/6J mice. *Appl. Anim. Behav. Sci.* **2016**, *184*, 135−140.

DOI: 10.1021/acs.inorgchem.8b02103
Inorg. Chem. 2018, 57, 15079−15092